Coordination Chemistry Reviews 477 (2023) 214954

Contents lists available at ScienceDirect

Coordination Chemistry Reviews

journal homepage: www.elsevier.com/locate/ccr

Review

# Metal-glycerolates and their derivatives as electrode materials: A review on recent developments, challenges, and future perspectives

Josué M. Gonçalves [a,b,*], Artur Luís Hennemann [b], José G. Ruiz-Montoya [c], Paulo R. Martins [d], Koiti Araki [b], Lúcio Angnes [b,*], Reza Shahbazian-Yassar [a,*]

[a] Department of Mechanical and Industrial Engineering, University of Illinois at Chicago, Chicago, IL 60607, United States
[b] Instituto de Química, Universidade de São Paulo, Av. Prof. Lineu Prestes 748, 05508-000 São Paulo, SP, Brazil
[c] Laboratorio de Investigación de Electroquímica Aplicada, Facultad de Ciencias, Universidad Nacional de Ingeniería, Av. Túpac Amaru 210, Rímac, Lima, Peru
[d] Instituto de Química, Universidade Federal de Goiás, Av. Esperança s/n, 74690-900 Goiânia, GO, Brazil

ARTICLE INFO

*Article history:*
Received 26 June 2022
Accepted 19 November 2022
Available online 8 December 2022

*Keywords:*
Metal-glycerolates
Supercapacitors
Batteries
Water-splitting
Oxygen evolution reaction
Hydrogen evolution reaction

ABSTRACT

The need for alternative forms of energy conversion and storage requires preparation of novel nanostructured material architectures. The emerging metal-glycerolates and their derivatives are promising classes of materials that can be prepared in various morphologies including porous, hollow, or yolk-shell structures. Such materials encompass a vast compositional space spanning from metal oxides to metal hydroxides, metal sulfides, and metal phosphides. This review addresses the synthesis of micro- and nanostructures derived from metal-glycerolate, using different preparation processes, as well as the applications of these materials, especially for the preparation of supercapacitors and batteries electrodes, as well as electrocatalysts for water splitting. In fact, the utilization of metal-glycerolates and their derivatives as electrode materials is a very recent theme attested by the fact that about 85% of the references reported in this review are published in the 2018–2022 period. In addition, the developments, challenges, and future perspectives as well as the future directions of these promising materials are discussed.



**Contents**



* Corresponding authors at: Department of Mechanical and Industrial Engineering, University of Illinois at Chicago, Chicago, IL 60607, United States (J.M. Gonçalves).
*E-mail addresses:* josuefisicoquimico@hotmail.com (J.M. Gonçalves), luangnes@iq.usp.br (L. Angnes), rsyassar@uic.edu (R. Shahbazian-Yassar).

https://doi.org/10.1016/j.ccr.2022.214954
0010-8545/

## 1. Introduction

Nowadays, there is a consensus that the ever-growing energy requirements of modern society cannot be supplied only by nonrenewable energy resources. In addition, the environmental problems caused by them are worsening and the daily lives of the population are being gradually impaired in a larger extent [1]. Therefore, there is an ever-growing and extremely urgent demand for sustainable and green renewable energy sources [2]. Another challenge is the development of energy technologies that are not subject to weather, unpredictable environmental changes, and intermittent characteristics [1,2]. In this context, the development of electrode materials and devices for energy conversion and storage is the key towards a more sustainable society. In fact, the performance of the green energy-related technologies is mainly determined by the materials that comprise them [1].

Among the promising hot topics in energy-related technologies, the development of new materials for supercapacitors and rechargeable batteries, as well as the preparation of electrocatalysts for water-splitting and fuel cells have received significant attention in recent years. In fact, the design of transition metal-based nanomaterials with the desired size, shape and composition is a reality and a growing trend in research around the world. Fortunately, as a result of such an effort, transition metal based materials showing impressive electrochemical performances have been prepared [2–5] generating interesting perspectives to replace noble metal based materials.

The promising progress of energy-related electrode micro/-nanomaterials is closely related to the variety of synthesis methods currently available such as solid-state reaction approach, sol–gel, hydrothermal treatment, electrodeposition, mechanochemical method, and so on. Furthermore, many groups have focused their attention on the development of new nanomaterials based on transition metals employing the sacrificial template approach associated with different thermal and/or chemical treatment methods. For instance, metal–organic frameworks (MOFs) are being extensively reported as ideal sacrificial templates, or precursors, for electrochemical sensor [6,7], energy storage [8] and energy conversion materials [9] due to their unique architectures characterized by huge surface areas, high porosity, and adjustable structures, into which is possible to add heteroatoms in a controlled way while preserving their structure, thus enhancing or incorporating new features. All those characteristics are essential for the rational design of multifunctional electrode materials [6,9].

Recently, metal-glycerolate (M−glycerolate) has been used as sacrificial templates/precursors in the preparation of various materials such as metal oxides, metal hydroxides, metal sulfides, metal phosphides and many more. In fact, glycerol is a biobased largely available, biodegradable, non-toxic, low vapor pressure, high boiling point, and non-flammable product (a coproduct from the biodiesel industry), that also is fully miscible with water. In the neutral form, the three hydroxyl groups impart high polarity to the molecule, but their coordination capacity is low, likewise other alcohol derivatives. However, this is very much improved by deprotonation generating alcoholate groups, a quite strong base and a much better ligand. In other words, the glycerolates species can present suitable coordination properties to produce structured nanomaterials acting as a chelating agent [10]. However, it is important to highlight that many of those coordination compounds have been mistakenly denominated M−glycerates in the literature. The similarity of the words glycerolate and glycerate probably was responsible for such situation (Fig. 1). Glycerate anion is the conjugate base of glyceric acid, which is a natural three-carbon sugar acid obtained from the oxidation of glycerol, whereas glycerolate refers to the anionic species resultant from deprotonation of glycerol, i.e., completely different chemical species. In this sense, our first contribution in this review is to call the attention of the readers, aiming to correct this unfortunate mistake. Therefore, in this work we will only use the term "M−glycerolate" to refer to the precursor of the different electrode materials that will be described here. In fact, a variety of nanostructures based on or derived from M−glycerolates were reported, being commonly used as precursors in the preparation of very promising porous, hollow, or yolk-shell nanomaterials for application in supercapacitors and batteries, as well as in electrocatalysis (Scheme 1). M−glycerolates refers to metal alkoxides consisting of stacked layers of glycerol (a polyalcohol) coordinated to metal ions. These hybrid inorganic–organic materials, combining the advantages of polyalcohol molecules and metal ions, exhibit substantial stability, high performance and tunable morphology and composition [11]. For instance, Liu *et al.* [12] summarized the advances achieved on the preparation of water splitting electrocatalysts by using a variety of metal-alkoxides and their derivatives as precursors.

As far as we know, there is no review work describing the promising results on the synthesis and applications of M−glycerolates and their derivatives as electrode materials in different energy technologies. Therefore, the recent progress in M−glycerolate or M−glycerolate−derived electrode materials for application in electrochemical energy technologies, especially as electrode materials for supercapacitors and batteries, as well as the current trends as electrocatalysts for water-splitting were highlighted. Finally, the challenges and perspectives in this field as well as the future directions are presented in this review.

## 2. General features and synthesis protocols of metal-glycerolates and derivatives

### 2.1. Metal-glycerolates

M−glycerolates are composed of two fundamental components, glycerolate anions and metal ions, and can be classified as inor-

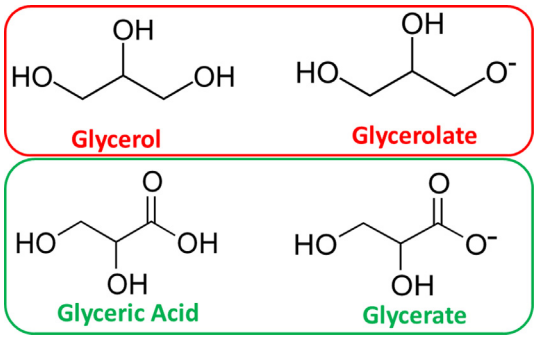


**Fig. 1.** Wire and frame structure of glycerol, glycerolate ion, glyceric acid, and glycerate ion.

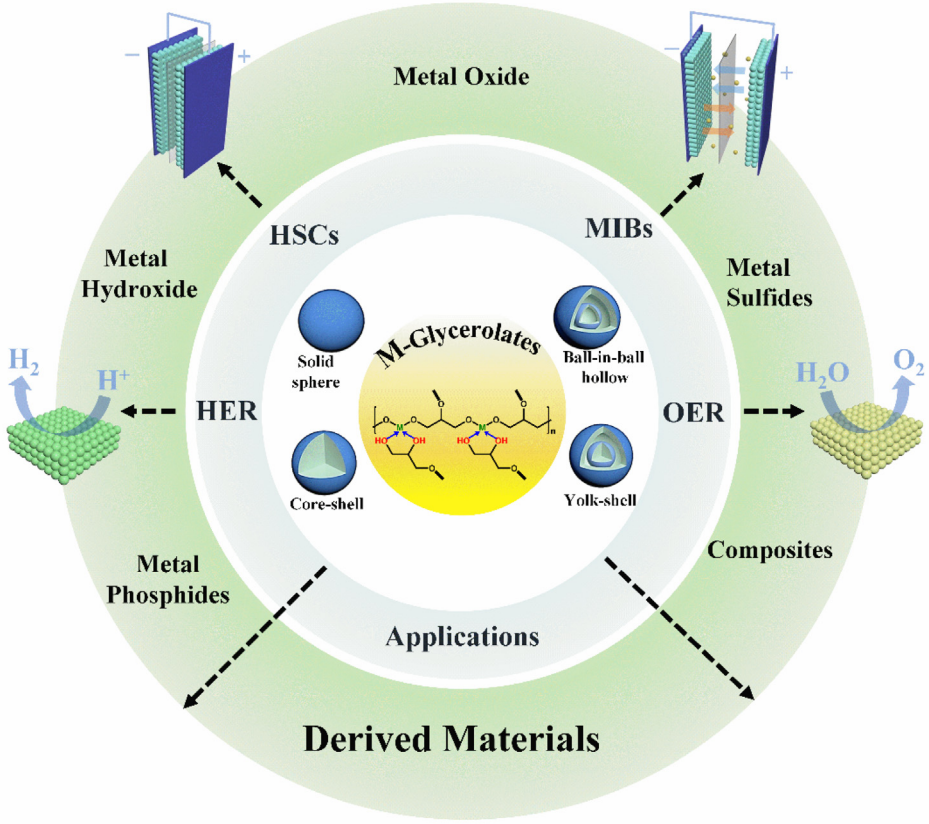


**Scheme 1.** Different types of micro/nanomaterials (metals, metal oxide/hydroxide, metal sulfides, metal phosphides, carbons, or their composites) prepared from M−glycerolate precursors for different applications (MIBs = metal-air batteries, HSCs = hybrid supercapacitors, HER = hydrogen evolution reaction, and OER = oxygen evolution reaction). A representative M−glycerolate structure and the preparation scheme of M−glycerolate microsphere *via* solvothermal method shown in the center of the scheme were adapted with permission from ref. [111]. Copyright © 2019 Science China Press. Published by Elsevier B.V. and Science China Press. All rights reserved.

ganic polymers combining the features of organic and inorganic materials, likewise MOFs and other metal alkoxides [12]. For example, a few isostructural 3*d* M−glycerolates with doubly-deprotonated glycerolate ligands were determined by single-crystal X-ray diffractometry, such as $Co(C_3H_6O_3)$ [13], $Zn(C_3H_6O_3)$ [14] and $Pb(C_3H_6O_3)$ [15]. More recently, Teichert *et al.* [16] reported the synthesis and characterization of $Sn_5(C_3H_5O_3)_4$, whose $Sn^{2+}$ and $Sn^{4+}$ ions are linked by triply-deprotonated $(C_3H_5O_3)^{3-}$ ligands (Fig. 2**A**). The 3D coordination network structure shows each O atom of the ligand bridging two Sn atoms, leading to a $\mu_4$-bridging coordination mode of $(C_3H_5O_3)^{3-}$ (Fig. 2**B**), where the $Sn^{4+}$ ion has a triangular dodecahedron shaped holo-directed $SnO_8$ coordination environment, while the lone-pair ion $Sn^{2+}$ displays hemi-directed $SnO_4$ coordination (Fig. 2**C**). In addition, Khonina *et al.* [17] reported the synthesis of $Fe^{2+/3+}$-glycerolates (Fig. 2**D**) which were characterized by Mossbauer and infrared spectroscopy, X-ray diffraction (XRD) and elemental analysis. However, unlike MOFs, the overwhelming majority of M−glycerolates have low crystallinity and are characterized by their amorphous nature. On the other hand, the phase structure of the M−glycerolates usually presents a XRD pattern exhibiting a low-angle reflection peak related to bonded glycerolate anion layers and stacked metal–oxygen layers, which are similar to the common transition metal-based hydroxides [12,18,19].

Interestingly, in contrast with MOFs, there is a lack of data demonstrating the formation mechanisms of micro- and nanomaterials based on M−glycerolates, since most of the works focus on the application of M−glycerolates or their derivatives, indicating that there is much to be explored in order to fully understand the properties and design of new M−glycerolate based materials.

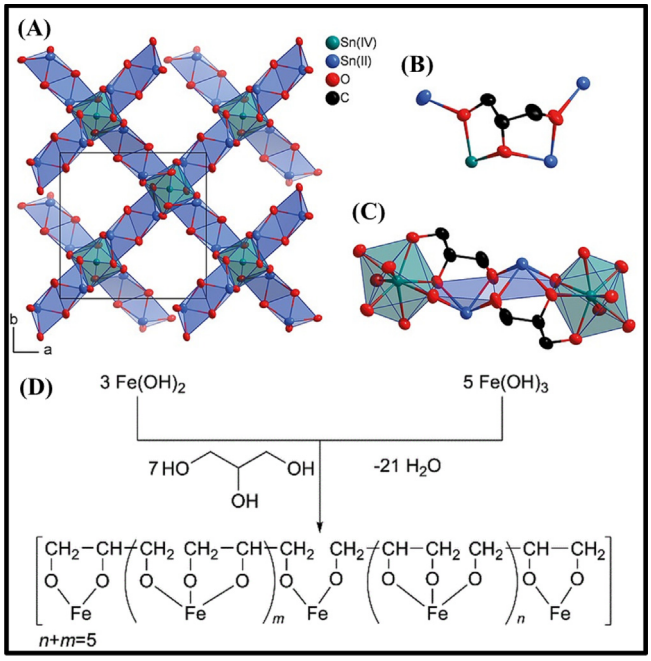


**Fig. 2.** (A) Crystal structure of $Sn_5(C_3H_5O_3)_4$, showing a (B) $\mu_4$-bridging mode of the $(C_3H_5O_3)^{3-}$ ligand, and (C) edge-linked $SnO_8$ and $SnO_4$ polyhedral structures. Reproduced with permission from ref. [16]. Copyright © 2019 The Authors. Published by Wiley-VCH Verlag GmbH & Co. KGaA. (D) Structure of a $Fe^{2+/3+}$–glycerolate. Reproduced with permission from ref. [17]. Copyright © 2022 The Author(s). Published by the Royal Society of Chemistry.

The synthesis of M−glycerolates is generally carried out by mixing a metal source (such as chlorides, nitrates, and acetates) with glycerol in solvents such as isopropanol, and alcohol among others [20], and subjecting to a solvothermal reaction typically in the temperature range of 140–250 °C [12,20]. The M−glycerolates prepared in this way are normally obtained as solid spheres with uniform size distribution (monodisperse) and good stability due to the protection of organic ligands [20]. However, the type of metal ion, structure of alcohol molecules and concentration, as well as the presence of additives can affect the composition and morphology of metal alkoxides [19], including M−glycerolates [12,19]. For instance, Zn-based M−glycerolates generally have plate-like [21] or microstacks [22] morphologies with high crystallinity.

An important similarity of M−glycerolates with the chemistry of MOFs is that both are excellent sacrificial templates/precursors for the design of micro/nanomaterials [6]. In fact, M−glycerolates derived materials have recently been reported as excellent precursors for the preparation of versatile, and multifunctional porous metal oxides, metal hydroxides, metal sulfides, metal phosphides, and metal carbides with homogeneous structures [20], as will be discussed in the next topic.

### 2.2. Metal-glycerolates derived materials

It is important to highlight that the analogy between MOFs and M−glycerolates extends beyond composition and morphology, as the similarities are also present in their properties and applications. For instance, despite the attractive properties of M−glycerolates (and MOFs), M−glycerolates only partially meet the requirements as advanced electrode materials for energy application. In fact, realistic applications of M−glycerolates based electrodes [6] are largely dependent on improvements of conductivity and the design of redox-active sites, essential features that must be satisfied for all electrode materials. In this context, the design of M−glycerolate derived materials have shown great promise, exhibiting exceptional conductivity, electrochemical activity, and stability. In addition, compared with MOFs (for example ZIF-67), the proportion of Co ions in Co-glycerolate sphere is much higher [23], which can result in nanocrystalline oxides with much higher Co concentrations and more stable porous structures that can resist to oxidation without any structural deterioration [23]. From this perspective, some strategies have been used in the synthesis of M−glycerolate derived materials to achieve the desired composition and porous structures, as presented below.

Generally, the synthesis of electrode materials derived from M−glycerolates can generate four usual types of morphologies: hollow spheres, yolk shelled hollow spheres, ball-in-ball hollow spheres and 2D laminar structures. In all cases, first the M−glycerolates are subjected to an anion exchange process to form metal hydroxides [24], metal oxides [25–27], metal sulfides [28–31], metal phosphides [32,33], metal selenides [34], among others. At this point, it is important to emphasize that the resultant material's

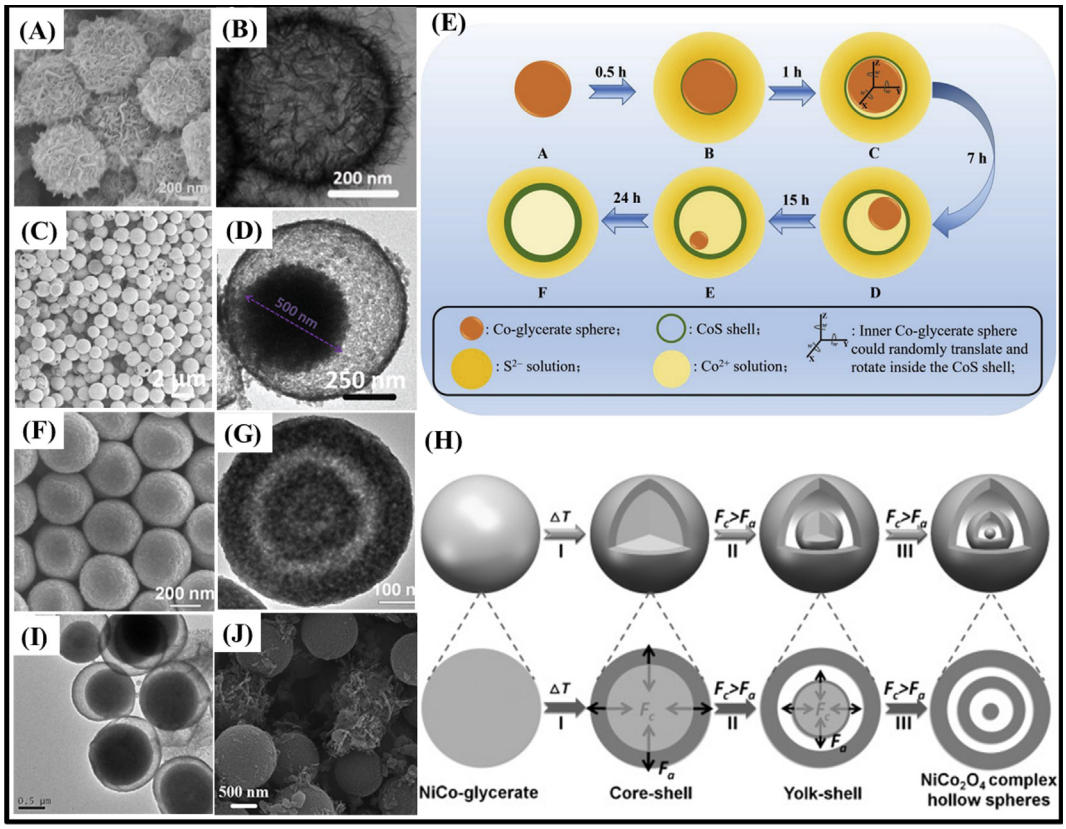


**Fig. 3.** (A-B) SEM and TEM images of hierarchical NiMn-hydroxide hollow spheres Reproduced with permission from ref. [24]. Copyright © 2020 Elsevier ltd. All rights reserved. (C-D) SEM and TEM images of NiCoMn-sulfide yolk-shell hollow spheres. Reproduced with permission from ref. [28]. Copyright © the Partner Organizations 2019. (E) Schematic illustration of the synthesis of CoS hierarchical porous nanospheres. Reproduced with permission from ref. [36]. Copyright © 2018 Elsevier B.V. All rights reserved. (F-G) SEM and TEM images of $NiCo_2O_4$ core-in-double-shell hollow spheres. (H) Schematic illustration of the formation process of $NiCo_2O_4$ core-in-double-shell hollow spheres. Reproduced with permission from ref. [27]. Copyright © 2015 WILEY-VCH Verlag GmbH & Co. KGaA, Weinheim. (I-J) SEM and TEM images of $MnCoS_4$ pinecone-like structures. Reproduced with permission from ref. [31]. Copyright Marketplace™, Royal Society of Chemistry.

structure is strongly dependent on parameters such as temperature, heating rate, solvents, pH, ion concentration, and time of reaction [24,27,29,35], that must be carefully controlled to yield a specific product.

Examples of the four types of possible structures are shown in Fig. 3. The spherical structure of NiMn-hydroxide is clearly shown in the SEM image (Fig. 3**A)** but the hollow structure, with a thin shell and an empty core, is only revealed by the TEM image. The low stability of M−glycerolate in water and 1-methyl-2-pyrrolidone is responsible for the transformation (anion etching) of NiMn-glycerolates to hierarchical NiMn-hydroxide hollow spheres after 10 h of reaction [24]. In addition, there have been reports that just a heat treatment can be enough to generate metal oxide hollow spheres [25,26].

A clear void between the outer shell and the inner sphere, characteristic of yolk-shell structure, is clearly shown in the TEM image of NiCoMn-sulfide **(**Fig. 3**D**), synthesized by sulfidation of MnCoNi-glycerolate with thioacetamide forming $Co_3S_4$, $Ni_3S_2$ and MnS spheres (Fig. 3**C**) [28]. It is important to mention that metal sulfide yolk-shell structures are an intermediate state in the ion exchange process since the yolk tends to be continuously transferred to the shell increasing its thickness, as illustrated by the mechanism called "Brownian-snowball" [36]. For example, Zhao *et al.* [36] reported that the Co-glycerolate inner nanospheres disappeared after sulfidation for 24 h, resulting in a hollow cobalt sulfide sphere with a thicker shell (Fig. 3**E**). In fact, the diameter of the inner structure of the yolk-shell CoS hierarchical porous nanospheres could be controlled accurately by the sulfidation time, temperature and concentration of reagents used in the solvothermal reaction [36].

Nevertheless, more complex structures denominated core-in-double-shell or ball-in-ball hollow spheres were achieved with $NiCo_2O_4$, as shown in the TEM image of Fig. 3**G** while the SEM image is shown in Fig. 3**F**. A solid core of 40 nm inside a hollow sphere of 200 nm that in turn is inside another 400 nm diameter hollow sphere can be clearly seen in Fig. 3**G**, as schematically shown in Fig. 3**H**. In this structure, the large gradient temperature generates contraction and adhesion actions ($F_c$ and $F_a$, respectively) in opposite directions. $F_c$ is associated with the degradation of organic species decreasing the M−glycerolate region, whereas $F_a$ hinders the inward contraction of the precursor core. The dynamic equilibrium of $F_c$ and $F_a$ controlled by temperature and time, can originate core–shell, yolk-shell and ball-in-ball hollow spheres structures (Fig. 3**H**) [27,29].

The yolk-shell hollow spheres of $MnCoS_4$ shown in Fig. 3**I** were converted into agglomerates of sheets (Fig. 3**J**) generating complex pinecone-like structures. Such a transformation was the consequence of reconstruction of the outer shell into thin sheets after more than 2 h of reaction, but preserving the inner core structure [31]. Nevertheless, M−glycerolates can be reacted with water to generate MnCo-hydroxide 2D hierarchical structures [35], in a similar way as in the preparation of NiMn-hydroxides hollow spheres (Fig. 3**B**), by using a suitable amount of water, reaction time and temperature to induce a controlled reconstruction of their particles.

More recently, core–shell structure preparation has also been reported [37]. In this work, a Co-glycerolate@nickel hydroxidenitrate microsphere (CoG@$Ni_3(NO_3)_2{\cdot}(OH)_4$) with core–shell structure is prepared by a simple two-step hydrothermal method. In more detail, after the synthesis of CoG, the second step to synthesize CoG@$Ni_3(NO_3)_2{\cdot}(OH)_4$ microspheres consisted of the reaction between CoG and $Ni_3(NO_3)_2{\cdot}6H_2O$ in isopropanol, which was autoclaved and kept at 180 °C for 12 h in an electric oven. After natural cooling, the aquamarine precipitate was washed 3–5 times with distilled water and ethanol dried overnight [37]. Despite the interesting results, based on our opinion, the shell formation mechanism is not only about the growing of $Ni_3(NO_3)_2{\cdot}(OH)_4$ on the surface of these CoG nanospheres, but also the ion exchange process since the core tends to be continuously transferred to the shell (increasing its thickness), resulting in the formation of $Co_3(NO_3)_2{\cdot}(OH)_4$ and/or $(NiCo)_3(NO_3)_2{\cdot}(OH)_4$, as confirmed by the significant presence of $Co^{2+}$ ions on the shell surface as shown in the XPS survey spectra.

## 3. Background in energy storage systems and water-splitting

### 3.1. Supercapacitors

Among the energy storage devices, supercapacitors (SCs) have attracted a lot of attention since present higher power density, faster charge/discharge, and longer life cycling stability but with lower energy density [38] as compared to batteries. They are classified as Electric Double Layer Capacitors (EDLCs) and pseudocapacitors depending on the electrode material and charge storage mechanism. EDLCs are based on carbon materials such as carbon nanotubes, graphene, and activated carbon, and their capacitance is purely non-Faradaic, associated to the electric charge accumulation in the electrode/electrolyte interface **(**Fig. 4**A)**. In contrast, pseudocapacitors rely especially on Faradaic processes [39] taking place at electroactive species such as metal oxides, nitrites, and conducting polymers [40–42] **(**Fig. 4**B)** but also on non-Faradaic electric double layer charge/discharge processes.

The electrochemical signature (CV and GCD) of EDLC and pseudocapacitor electrode materials are very similar, both exhibiting a rectangular profile within a potential range, and a linear potential decrease as a function of time during a galvanostatic discharge at constant current (Fig. 4**D**). In contrast, battery-type materials have a purely Faradaic electrochemical behavior, i.e., the charge storage mechanism is associated with redox reactions controlled by diffusional processes (Fig. 4**C**), characterized by well-defined pair of waves as signature in the cyclic voltammograms. Furthermore, the potential remains almost constant during the galvanostatic discharge curve while the redox process takes place, then suddenly falling down, as shown in Fig. 4**D**. Nevertheless, battery-type materials have been mistakenly classified as pseudocapacitors by some authors that are using F $g^{-1}$ (typical of EDLCs and pseudocapacitors) [43] instead of C /$g^{-1}$ or mAh $g^{-1}$ as the charge capacity metric for battery-type materials.

Supercapacitor devices can be further classified into three types according to the cathode and anode material: symmetric, asymmetric and hybrid. Symmetric devices have the anode and cathode made of the same material, either with EDLC or pseudocapacitive materials such as graphene//graphene and $RuO_2$//$RuO_2$ [44,45], as depicted in Fig. 4**E**. In contrast, the negative and positive electrodes of asymmetric devices [46] are made of different materials, which can be EDLC or pseudocapacitive materials such as activated carbon and $MnO_2$, as shown in Fig. 4**F**. Finally, the hybrid supercapacitor device combines a capacitive or pseudocapacitive material with battery-type materials such as $Ni(OH)_2$ and NiO [47] (Fig. 4**G**). This approach seems to be more interesting because the positive characteristics of each type of electrode material can be combined to assemble energy storage devices with exceptional electrochemical performance. In fact, battery-type materials can provide high energy density while pseudocapacitive materials provide high power density and longer life cycles.

### 3.2. Rechargeable batteries

Unlike capacitors and supercapacitors, battery cells have high specific capacity values (mA h $g^{-1}$), and high gravimetric (W h

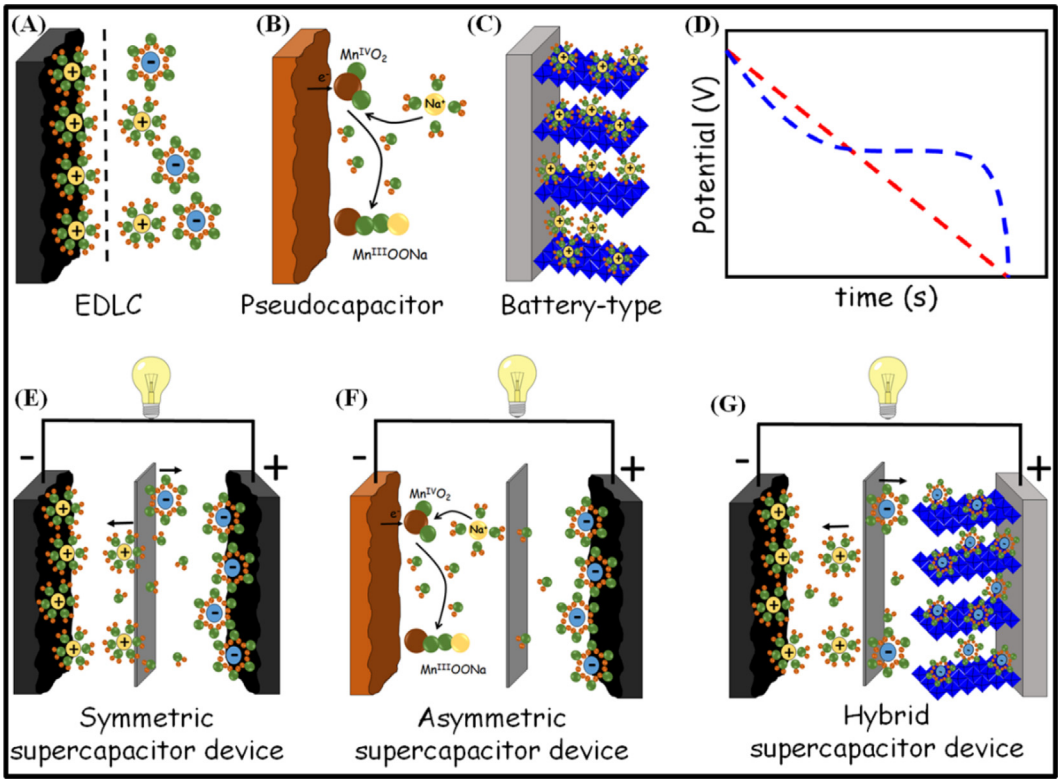


**Fig. 4.** Schematic representation of a typical EDLC (A), pseudocapacitor (B), and battery-type material (C). Galvanostatic discharge curves (D) of EDLC/pseudocapacitor (red dashed line) and battery-type materials (blue dashed line). Schematic representation of the types of supercapacitor devices: symmetric (E), asymmetric (F), and hybrid (G). (For interpretation of the references to colour in this figure legend, the reader is referred to the web version of this article.)

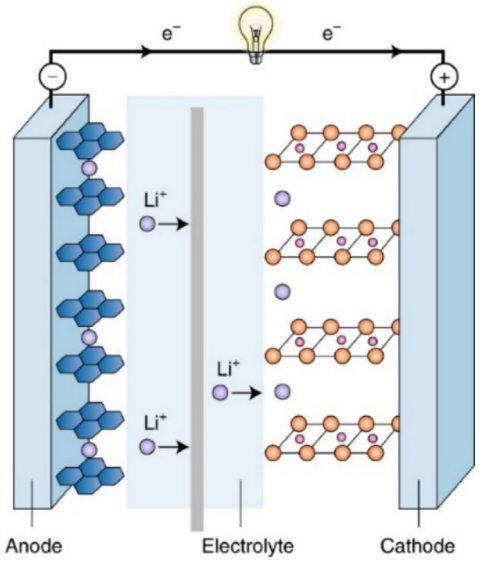


**Fig. 5.** Components and operation of a rechargeable Li-ion battery. Reproduced with permission from ref. [53]. Copyright © 2018 Macmillan Publishers Limited, part of Springer Nature. All rights reserved.

$Kg^{-1}$) and volumetric ($W\,h\,L^{-1}$) energy densities values. Basically, a battery can store electrical energy in the form of chemicals and redox reactions (faradaic charge transfer processes), providing direct current electricity as shown in Fig. 5 [48]. During charging of battery electrodes, ions are deintercalated from the cathode material and diffuse to the anode *via* the electrolyte medium, which is a conductor for ions and an insulator for the electrons generated at the cathode, and permits the redox reaction on both electrodes [48], while the electrons reach the anode material *via* an external circuit, whereas discharging reverses this process. Thus, specific capacity obtained in battery electrodes is limited by solid-state ion diffusion, exhibiting relatively poor kinetics; however, the use of the entire bulk of the electrode for charge storage leads to very high energy density [49–52].

Among several different energy storage technologies, metal-ion batteries, in particular lithium-ion batteries (LIBs) have currently been accepted as the leading candidate for commercial electrochemical energy storage systems (EESSs). In fact, the LIBs have played a dominant role in promoting the development of the portable device market, electric vehicles, and aerospace due to their high energy density, high output voltage, long life, simple maintenance, and environmentally friendly operation [54–56]. In addition, the success of LIBs so far can be largely attributed to their high gravimetric ($\sim$100–265 $Wh\,kg^{-1}$) and volumetric energy density ($\sim$250–670 $Wh\,L^{-1}$) [57]. However, the high demand and extraction of lithium have experienced a significant rise over the last years [58], where the cost tends to be high due to the concentration of strategic resources of key metals (Li, Co, etc.) in few countries that are susceptible to geopolitical issues [57,59].

On the other hand, the sodium source in earth is much richer than lithium in earth's crust, being widely dispersed around the planet and low cost [56], therefore, sodium-ion batteries (SIBs) have gained considerable attention in the application of large-scale stationary electrical energy storage. $Li^+$ and $Na^+$ cations are neighbors in the alkali metals group and both have one loosely bound electron in their outer shell with analogous chemical properties, which similar standard electrode potentials: –2.71 V *vs* SHE for $Na^+$/Na and –3.04 V *vs* SHE for $Li^+$/Li [58]. However, the practical implementation of SIBs as mobile devices and the vehicle transportation sector can be a limiting factor due to the lower energy

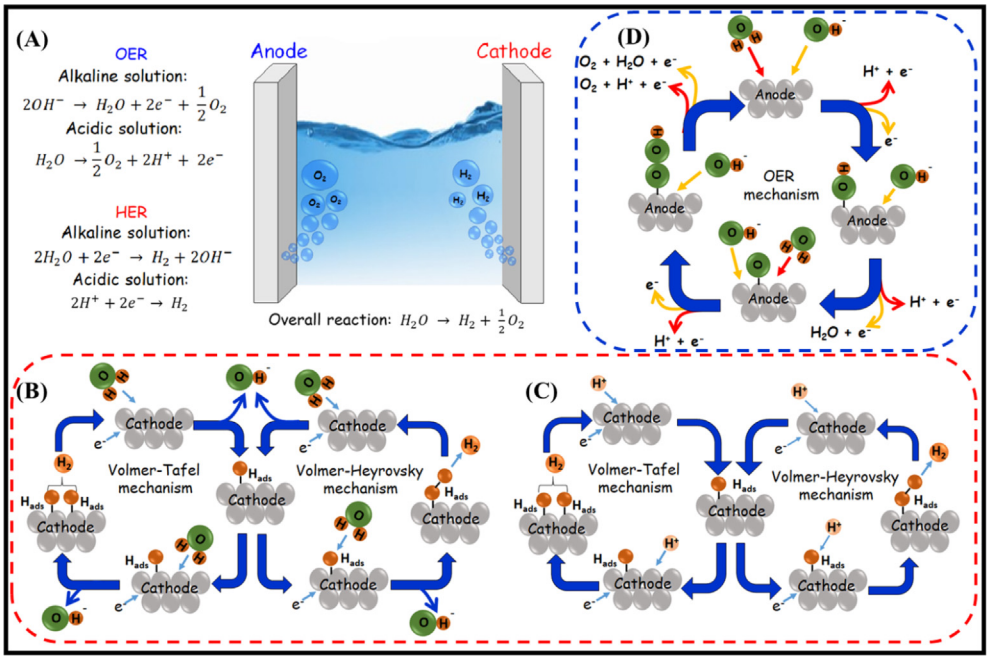


**Fig. 6.** Schematic representation of a water-splitting system and the OER and HER reactions in alkaline and acidic conditions (A). HER mechanism in alkaline (B) and acidic solution (C), and respective OER mechanism (D) in alkaline (orange arrows) and acidic solution (red arrows). (For interpretation of the references to colour in this figure legend, the reader is referred to the web version of this article.)

density, not being a problem to be used in massive storage applications such as grid energy storage where energy density is not a crucial factor [58]. Despite the great advances achieved and the knowledge that sodium-ion batteries will play an important role in energy management in the future, the scientific community recognizes that much research is needed to overcome the inherent limitations of sodium as a guest species and electroactive element [60].

It is important to mention that many review works already published highlighting recent progress, issues and challenges in the designer electrode materials, electrolyte, and interfaces for rechargeable LIBs [61–65], as well as rechargeable SIBs as potential alternatives to current LIBs [56,57,66], which can be used to obtain more detailed information about these EESSs.

### 3.3. Water-splitting

Over the years, it has become increasingly obvious that obtaining energy from non-renewable sources has brought serious problems to our planet as well as the people who live on it. In this sense, the development of clean and sustainable energy is necessary due to the environmental pollution and depletion of non-renewable sources caused by the increasingly high energy demand [67,68].

Hydrogen is one interesting alternative to fossil fuels since it has a high energy density (120 – 142 MJ/kg) [69] and is environmentally safe because water is its only combustion product. Currently, more than 95 % of the world's hydrogen demand is met by reforming of natural gas, gasification of coal and oil since hydrogen fuel is not available in nature [70,71]. Nevertheless, those processes are responsible for the emission of large amounts of greenhouse gases and consumption of extensive amounts of fossil fuels. An appealing approach to circumvent those drawbacks is producing high purity hydrogen (greater than99.9 %) by clean and sustainable water-splitting process [72].

The water-splitting reaction ($2H_2O \rightarrow H_2 + O_2$) can be carried out by photocatalytic and electrocatalytic processes. The first is the most desirable one but still technologically challenging conversion of solar to chemical energy. In contrast, the electrochemical water-splitting, as discussed earlier, converts electricity into chemical energy by promoting simultaneously the hydrogen and oxygen evolution reactions. As can be seen in Fig. 6**A**, the overall water-splitting process can be separated in two half-electrode reactions: the hydrogen evolution reaction (HER) at the cathode and the oxygen evolution reaction (OER) at the anode [73]. In order to provide abundant $H^+/OH^-$ ions and improving the electrocatalytic process, the electrolyzer operates with water under extreme acidic or alkaline pH conditions such as pH 1 – 4 or pH 11 – 14 [74], whose equations are displayed in Fig. 6**A**. The detailed mechanisms of HER and OER and some important water-splitting parameters are discussed below.

#### 3.3.1. Hydrogen evolution reaction (HER) and oxygen evolution reaction (OER)

The HER mechanism involves two electron-transfer processes, both in alkaline and acidic media, and the production of molecular hydrogen can be summarized in three steps, as illustrated in Fig. 6**B and 6C**. Firstly, hydrogen species are adsorbed on the catalyst surface either from the cleavage of the O—H bond of the water (alkaline medium) or direct from the abundant $H^+$ species present in acidic solution. That first step called Volmer reaction is a common step in HER, regardless of the medium used (alkaline or acidic). Then, two adsorbed hydrogen species ($H_{ads}$) react with each other, or with $H^+$ species in solution forming a H—H bond, generating molecular hydrogen through the Volmer-Tafel or the Volmer-Heyrovsky pathway that finally detaches from the catalyst surface. Despite the similarity of the HER reaction in both conditions, the rate in alkaline is two orders of magnitude lower than in acidic conditions [75].

The OER is the other half-reaction that takes place concomitantly and the rate-limiting reaction of the overall water-splitting process involves the transfer of four-electrons, the break of two O—H bonds and formation of a O=O bond in acidic medium. The OER mechanism in acidic (red arrows) and alkaline (orange arrows) conditions is presented in Fig. 6**D** showing that the oxygen

evolution is preceded by the oxidation of hydroxide ion or water molecule respectively under alkaline and acidic conditions [76]. Also, when compared to the HER mechanism, the OER has more intermediate species (such as O*, OH*, and OOH*) than HER ($H_{ads}$ or $H^+$). Accordingly, the OER process is significantly more sluggish thus demanding extra energy to take place at suitable rate, i.e., a higher overpotential is necessary to produce $O_2$.

*3.3.2. Key parameters in water-splitting electrocatalysis*

The performance or efficiency of an electrocatalyst to promote the HER at the cathode and the OER at the anode can be evaluated considering key parameters such as overpotential, Tafel slope, exchange current density, and stability of the electrodes in operation condition.

Although, the theoretical thermodynamic potential difference to drive the water-splitting is 1.23 V, under standard conditions (1 atm of $H_2$ and $O_2$, 298.15 K), in practice the potential that must be applied is much higher, in the range of 1.3 to 2.0 V, to overcome activation energy of both electrodes. The additional voltage (energy) that must be added to overcome the kinetic barrier is denominated overpotential ($\eta$). However, we should be aware that there are other factors contributing to the total applied voltage in addition to the anode ($\eta_a$) and cathode ($\eta_c$) overpotentials such as the resistance of the electrolyte and at the electric contacts. The overpotentials under a specified current density, for example of 10 mA $cm^{-2}$ ($\eta_{10}$), can be easily measured and used to evaluate the electrocatalytic performance of materials, where lower $\eta_{10}$ values indicate higher electrocatalytic activity [77].

The Tafel slope and exchange current density are two significant parameters that can be deduced from Tafel equation: $\eta = a + b \log j$. The Tafel slope "*b*" can be associated with the sensitivity of the current density to the applied potential and is inversely proportional to the heterogeneous reaction rate on the electrode surface. Consequently, the smaller the Tafel slope *b*, the less overpotential is required to supply the same current density increment, as expected for a higher reaction kinetics [78]. The electron transfer efficiency at the electrode/solution interface, denominated exchange current density ($j_0$), is the current density determined at zero overpotential [79] from the Tafel equation, under equilibrium condition. Thus, a good electrocatalyst must exhibit high $j_0$ and low Tafel slope *b* value, in addition to good chemical and mechanical stability.

Three are the methods to estimate the stability of an electrocatalytic material: chronoamperometry, chronopotentiometry and linear (or cyclic) voltammetry. The first one monitors the current at a constant applied potential, whereas the second monitors the potential at a constant current density. A decrease of current density at a given potential, or the need of a higher potential to keep a given current density indicates a lowering of the electrocatalytic activity. Generally, the current density should be equal or higher than 10 mA $cm^{-2}$ (most commonly used value), and the stability test must be carried out for periods longer than 10 h when considering perspectives of practical application. A good electrocatalyst must present small potential or current variation along the test. Another way to evaluate the durability of an electrocatalyst is by cyclic voltammetry or linear sweep voltammetry before and after the stability test. If the onset potential and overpotential at a constant current density remained more or less constant with no significant shift, then the electrocatalyst has good durability and stability.

## 4. Metal-glycerolates and their derivatives for supercapacitors

Electrode materials derived from M−glycerolates such as metal oxides, metal hydroxides, metal sulfides and metal phosphides have been reported as supercapacitor electrode materials, showing comparable or better electrochemical properties than their corresponding analogs (directly synthesized). For example, among the electrode materials listed in Table 1, hierarchical bimetallic NiMn-hydroxide hollow spheres [24] shows a superior specific capacitance of 1680 F $g^{-1}$ at 2 A $g^{-1}$, rate capability of 64 % (1068 F $g^{-1}$ at 15 A $g^{-1}$) while retaining 96.6 % of specific capacitance after 5500 charge/discharge cycles, at 10 A $g^{-1}$. In fact, NiMn-hydroxide hollow sphere derived from M−glycerolate showed higher specific capacitance than the more sophisticated rGO@NiMn-LDH@NF electrode material (1547 F /$g^{-1}$ at 2 A $g^{-1}$) [80] and other electrode materials based on NiMn-hydroxides [59,81]. These results can be explained by the: i) high surface area (140.68 $m^2$ $g^{-1}$) and mesoporosity enhancing the contact area of electrolyte with the electrode, ii) hollow architectures effectively enduring volume expansion during charge/discharge cycles, iii) presence of nanosheets in the outer shell minimizing the ion/electron diffusion, and iv) the amorphous layered structures further favoring the diffusion of ions/electrons.

Similarly, trimetallic NiCoMn-sulfide yolk-shell hollow spheres [28] show high specific capacitance of 1360 F $g^{-1}$ at 1.0 A $g^{-1}$, with exceptional rate capability of 88.5 % (2–10 A $g^{-1}$) and 92.6 % of capacitance retention after 6000 cycles at 4.0 A $g^{-1}$, that were ascribed to its relatively high surface area (106.1 $m^2$ $g^{-1}$) enhancing the accessibly of electrolyte. Moreover, the yolk-shell structure can efficiently accommodate volume expansion, reduce the diffusion and transmission path for electrolyte ions, and serve as a reservoir of ions.

$NiCo_2O_4$ core-in-double-shell hollow spheres [27] showed a 1141 F $g^{-1}$ at 1 A $g^{-1}$, a rate capability of 69 % (1–15 A $g^{-1}$) superior to many other $NiCo_2O_4$ electrodes (see reference [82] and references therein), and 94.7 % of capacitance retention over 4000 cycles. The unique three-layer core-in-double-shell inner structure and porous shell favor the easy insertion/extraction of electrolyte ions while buffering the large volume change associated with it [27].

$MnCoS_4$ pinecone-like structures [31] present intermediate values of specific capacitance (992 F $g^{-1}$ at 1 A $g^{-1}$) and rate capability (65 % from 1 to 20 A $g^{-1}$, and 75 % from 1 to 10 A $g^{-1}$, calculated from ref. 24), but exceptional capacitance retention of 102.35 % after 5500 cycles at 10 A $g^{-1}$. This material behaves as a 2D material with more restricted electrochemical properties as compared to spheres [32,35], as shown in the Table 1, where the performance of different materials as positive electrodes of supercapacitors is summarized. It is evident that the type of metal plays a key role in defining the efficiency of electrode materials. Accordingly, most electrode materials are based on Ni and Co, with much lower amounts based on Mn and only a few made of Cu as complementary metal. Among the materials considered in this review (metal oxides, metal hydroxides, metal phosphides and metal sulfides derived from metal-glycerolates), most of them have spinel-like structures, such as $Co_3O_4$ [27], $NiCo_2O_4$ [27], $CuCo_2O_4$ [25], $MnCo_2O_4$ [26], $Co_3S_4$ [83], $NiCo_2S_4$ [84], and $CuCo_2S_4$ [30]. Moreover, materials based on metal sulfides demonstrated superior rate capabilities especially when associated with the ball-in-ball structure. This tendency can be mainly attributed to their higher electric conductivity [9,85,86] and the core-in-double-shell structure buffering the large volume changes associated with the ion insertion/extraction process [27]. Also, it is important to note that most materials in Table 1 present charge retention on cycling above 90 % demonstrating good stability.

Some examples of composite materials derived from M−glycerolates by incorporation of a second component are shown in Fig. 7. For instance, PrGO/NiCoP [33] (Fig. 7**A-D)** is a material showing NiCoP particles supported on P-doped reduced graphene oxide (PrGO) synthetized by the reaction of NiCo-glycerolates with gra-

**Table 1**
Comparison of the relevant electrochemical parameters of M−glycerolates and their derivatives electrode materials and their performance in supercapacitor devices assembled with a suitable carbon cathode material.

| Electrode Material | Electrode Material Morphology | Collector electrode/ binder and solvent | Metal-glycerolate precursors | Three electrodes system | | | | | | Two electrodes system (device supercapacitor) | | | | Ref. |
|---|---|---|---|---|---|---|---|---|---|---|---|---|---|---|
| | | | | Specific Capacitance (F $g^{-1}$) | Specific Capacity (C $g^{-1}$) | Potential Window (V *vs* reference electrode) | Rate Capability in % retention (current density range) | Charge retention capacity % (number of cycles) | Electrolyte | Voltage window (V) | Energy Density (Wh $kg^{-1}$) | Power Density (kW $kg^{-1}$) | Negative Electrode Material | |
| **Ni-Mn hydroxide hollow spheres** | Hollow spheres | NF/(PVDF, acetylene black and IPA) | Ni-Mn | 1680 F $g^{-1}$ at 2.0 A $g^{-1}$ | – | 0 – 0.6 *vs* Hg/HgO | 64 % (2–15 A $g^{-1}$) | 96.6 % (5500 cycles at 10 A $g^{-1}$) | 3.0 M KOH | 0–1.65 V | 42.8<br>29.7 | 1.703<br>12.747 | AC | [24] |
| **$CuCo_2V_2O_8$** | Hollow sphere $CuCo_2V_2O_8$ | NF/(PVDF, acetylene black and NMP) | Cu-Co | – | 799.8 C $g^{-1}$ at 2 A $g^{-1}$ | −0.1 – 0.5 V *vs* Ag/AgCl | 60.65 % (2–50 A $g^{-1}$) | 96.5 % (7000 cycles at 2 A $g^{-1}$) | 3.0 M KOH | 0–1.6 V | 62.54<br>35.13 | 1.928<br>42.307 | AC | [25] |
| **$MnCo_2O_4$ Hollow Spheres** | Hollow spheres | Carbon Fibers (CF)/ (PVDF and acetylene black and NMP) | Mn-Co | 800 mF $cm^{-2}$ at 2 mA $cm^{-2}$ (200 F $g^{-1}$ at 0.5 A $g^{-1}$ **) | – | 0–0.4 V *vs* SCE | 52.5 % (2–40 mA $cm^{-2}$ or 0.5 – 10 A $g^{-1}$ **) | 99 % (2000 cycles at 40 mA $cm^{-2}$ or 10 A $g^{-1}$ **) | 1.0 M KOH | 0–1.2 V *** | 0.052 mWh $cm^{-3}$ ***<br>0.043 mWh $cm^{-3}$ *** | 32 mW $cm^{-3}$ ***<br>320 mW $cm^{-3}$ *** | AC | [26] |
| **NiCoMn sulfide yolk-shell HSs** | Yolk-shell hollow | NF/(PVDF and acetylene black) | Ni-Co-Mn | 1360 F $g^{-1}$ at 1.0 A $g^{-1}$ | – | 0 – 0.5 V *vs* Hg/HgO | 88.5 % (1–10 A $g^{-1}$) | 92.6 (6000 cycles at 4.0 A $g^{-1}$) | 3.0 M KOH | 0–1.7 V | 49.8<br>38.9 | 1.700<br>8.499 | AC | [28] |
| **$NiCo_2O_4$** | Core-in-double-shell hollow spheres | NF/Carbon black and PVDF | Ni-Co | 1141 F $g^{-1}$ at 1.0 A $g^{-1}$ | – | 0 – 0.6 V *vs* SCE | 69 % (1–15 A $g^{-1}$) | 94.7 % (4000 cycles at 5 $g^{-1}$) | 6.0 M KOH | – | – | – | – | [27] |
| **$NiCo_2S_4$ ball-in-ball hollow spheres** | Ball-in-ball hollow spheres (Core-in-double-shell hollow spheres) | NF/(carbon black and PVDF) | Ni-Co | 1036 F $g^{-1}$ (518F $cm^{-3}$) at 1 A $g^{-1}$ | – | −0.1 – 0.55 V *vs* SCE | 68.1 % (1–20 A $g^{-1}$) | 87 % (2000 cycles at 5 A $g^{-1}$) | 6.0 M KOH | 0–1.6 V | 42.3<br>22.9 | 0.476<br>10.208 | G/CSs | [29] |
| **$CuCo_2S_4$ ball-in-ball HNSs** | Ball-in-ball hollow spheres (Core-in-double-shell hollow spheres) | NF/(Carbon black, PVDF and NMP) | Cu-Co | 442 F $g^{-1}$ at 0.5 A $g^{-1}$ | – | 0 – 0.4 V *vs* Hg/HgO | 47.5 % (0.5–10 A $g^{-1}$) * | 84.5 % (5000 cycles at 5 A $g^{-1}$) | 2.0 M KOH | – | – | – | – | [30] |
| **CoS-9 h** | Ball-in-ball hollow spheres | NF/ethanol (no binder) | Co | 932F/g at 5 A $g^{-1}$ | – | 0 – 0.6 V *vs* SCE | 70 % (5–50 A $g^{-1}$) | Above 100 % (1000 cycles at 10 A $g^{-1}$) | 3.0 M KOH | – | – | – | – | [36] |

(*continued on next page*)

**Table 1** (*continued*)

| Electrode Material | Electrode Material Morphology | Collector electrode/ binder and solvent | Metal-glycerolate precursors | Three electrodes system | | | | | | Two electrodes system (device supercapacitor) | | | | Ref. |
|---|---|---|---|---|---|---|---|---|---|---|---|---|---|---|
| | | | | Specific Capacitance ($F\ g^{-1}$) | Specific Capacity ($C\ g^{-1}$) | Potential Window (V *vs* reference electrode) | Rate Capability in % retention (current density range) | Charge retention capacity % (number of cycles) | Electrolyte | Voltage window (V) | Energy Density ($Wh\ kg^{-1}$) | Power Density ($kW\ kg^{-1}$) | Negative Electrode Material | |
| **NiHPi-500** | 2D formed with Nanotubes of Nickel phosphate | Carbon Paper/(water/ ethanol and Nafion) | Ni | 450 F $g^{-1}$ at 1.0 A $g^{-1}$ | – | 0 – 0.45 V *vs* Ag/AgCl | 51.3 % (1–10 A $g^{-1}$) | 102.35 % (5000 cycles at 10 A $g^{-1}$) | 1.0 M KOH | 0–1.45 V | 50<br>32 | 0.362<br>2.838 | AC | [32] |
| **2D $NiCo_2O_4$NSs** | Two-dimensional mixed oxide nanosheets | Graphite substrate/ (PVDF, acetylene black and NMP) | Ni-Co | 200F/g at 5 mV $s^{-1}$ | – | −0.1 – 0.5 V *vs* Ag/AgCl | 62.5 % (5–100 mV $s^{-1}$) | – | 3.0 M KOH | 0–1.6 V | 38.53<br>21.05 | 0.299<br>0.34 | GO | [35] |
| **$MnCoS_4$** | Pinecone-like | NF/ethanol (no binder) | Mn-Co | 992 F $g^{-1}$ at 1 A $g^{-1}$ | – | 0 – 0.4 V *vs* Hg/HgO | 65 % (1–20 A $g^{-1}$) | 102.35 % (5500 cycles at 10 A $g^{-1}$) | 3.0 M KOH | – | – | – | – | [31] |
| **PrGO/NiCoP** | Hollow spheres of NiCoP embedded in PrGO | NF/(PVDF, acetylene black and NMP) | Ni-Co | 2586.9 F $g^{-1}$ at 1.0 A $g^{-1}$ | – | 0 – 0.5 *vs* Hg/HgO | 89 % (1–20 A $g^{-1}$) | 80 % (6500 at 30 A $g^{-1}$) | 3.0 M KOH | 0–1.7 V | 49.7<br>23.3* | 0.366<br>5.092* | AC | [33] |
| **$NiCo_2S_4$/2RGO** | Yolk-shelled $NiCo_2S_4$ hollow spheres on RGO films | Self-material sandwiched between two pieces of Ni foam with platinum foil as counter electrode/ binder free | Ni-Co | 1000.5 F $g^{-1}$ at 1.0 A $g^{-1}$ | – | 0 – 0.4 V *vs* Ag/AgCl | 62 % (1–10 A $g^{-1}$) | – | 6.0 M KOH | 0–1.6 V | 15.4<br>9.8 | 0.22<br>2.227 | AC | [84] |
| **α-MnS@$Co_3S_4$@NF** | Hollow sphere MS @ nanosheets of $Co_3S_4$ | NF/(PVDF, acetylene black and NMP) | Mn | – | 1019.9 C $g^{-1}$ at 1.0 A $g^{-1}$ | 0 – 0.5 V *vs* Ag/AgCl | 81.5 % (1–25 $Ag^{-1}$) | 92.74 % (10000 at 15 A $g^{-1}$) | 6.0 M KOH | 0–1.5 V | 54.9 | 0.753 | AC | [83] |
| **NiMn-Gly** | Microspheres | NF/(PVDF, acetylene black) | Ni-Mn | – | 719 C $g^{-1}$ at 1.0 A $g^{-1}$ | 0 – 0.4 V | ~60 % (1–20 $Ag^{-1}$) | 100 % (20000 cycles 10 A $g^{-1}$) | 3.0 M KOH | 0–1.6 V | 54.4 | 0.8 | AC | [89] |

Where: NF: Nickel foam, PVDF: polyvinylidene fluoride, IPA: isopropyl alcohol, NMP: *N*-methylpyrrolidone, AC: Activated carbon, PrGo: P-doped reduced graphene oxide, NiHPi: Nickel hydrogen phosphate, $NiCo_2S_4$/2rGO: mixture of $NiCo_2S_4$ and rGO in the mass ratio of 1: 2, NSs: nanosheets, HSs: hollow spheres, G/CSs: graphene/carbon spheres nanocomposite, HNSs: hollow nanospheres.
*: Data estimated from figure in the article.
**: Calculated from articles' data.
***: Solid-state electrolyte PVF-KOH.
-: No mention in the article.

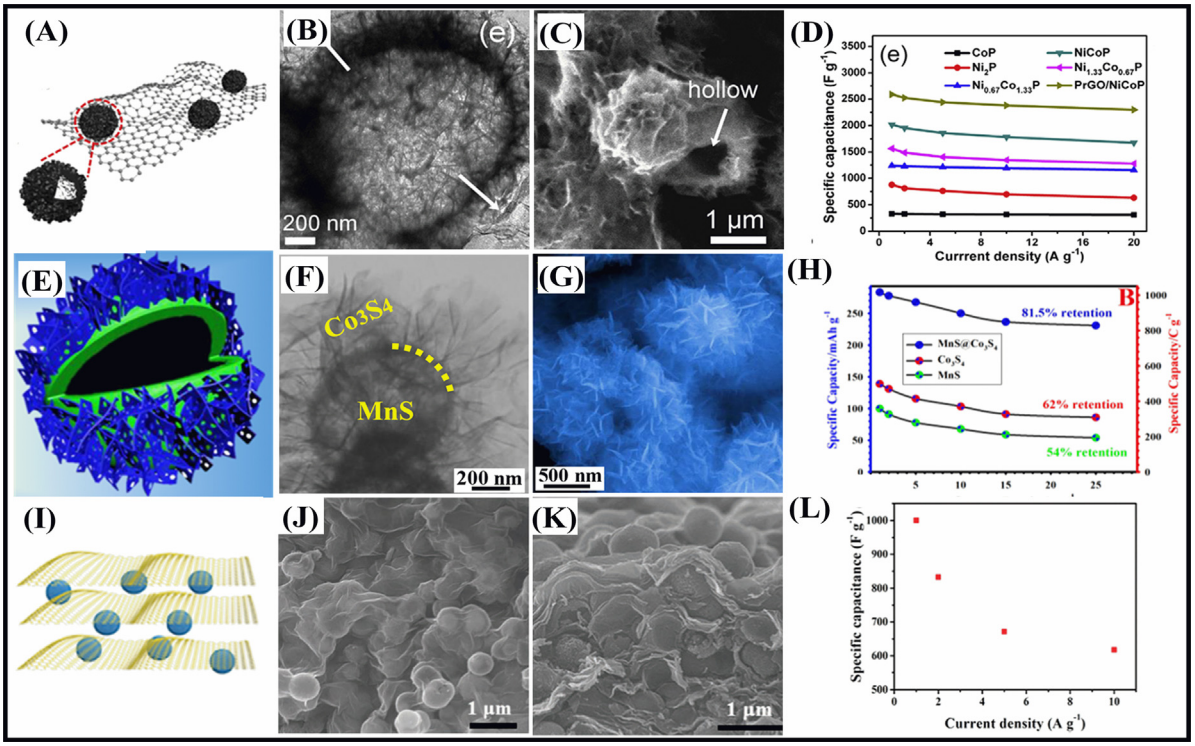


**Fig. 7.** Schematic representation of the structure, TEM and SEM images, and specific capacitance (or capacity) *vs* current density (rate capability) of: (A, B, C, D) PrGO/NiCoP. Reproduced with permission from ref. [33]. Copyright © 2019 Elsevier ltd. All rights reserved. (E, F, G, H) MnS@$Co_3S_4$. Reproduced with permission from ref. [83]. Copyright © 2021 Elsevier B.V. All rights reserved. (I, J, K, L) $NiCo_2S_4$/2rGO materials. Reproduced with permission from ref. [84]. Copyright © The Royal Society of Chemistry and the Centre National de la Recherche Scientifique 2018.

phene oxide (GO) in an autoclave, followed by a phosphorization reaction. PrGO/NiCoP showed the highest specific capacitance and rate capability respectively of 2596.9 F $g^{-1}$ and 89 % from 1 to 20 A $g^{-1}$ (Fig. 7**D**), that were assigned to the synergic effect of NiCoP and PrGO (both phosphorized), the hierarchical hollow structure with mesoporous structure and large specific area (294.3 $m^2$ $g^{-1}$). In addition, pseudocapacitive behavior predominates in the energy storage mechanism of PrGO/NiCoP [33].

The material α-MnS@$Co_3S_4$ (Fig. 7**E-H**) presented a specific capacity of 1019.9 C $g^{-1}$ at 1.0 A $g^{-1}$ and 81.5 % of rate capacity from 1 to 25 A $g^{-1}$ (Fig. 7**H**) [83], whereas $NiCo_2S_4$/2rGO [84] (Fig. 7**I-L**) showed a specific capacitance of 1000.5 F $g^{-1}$ at 1.0 A $g^{-1}$ and 62 % of rate capacity from 1 to 10 A $g^{-1}$ (Fig. 7**L**) [84]. These three examples demonstrate the synergic effect of metal sulfides or phosphides hollow spheres with highly conductive carbon materials as support improving the overall performance and durability of electrode materials.

Finally, the most relevant supercapacitor device parameters as well as the M−glycerolate precursor, the electrode material and morphology are also listed in the Table 1. The type of supercapacitor device, asymmetric or hybrid, can be deduced from the positive electrode and the carbon material of the negative electrode. The correlations of power density and energy density of the different electrode materials are shown in the Ragone plot (Fig. 8) where clearly the $CuCo_2V_2O_8$//AC supercapacitor device show the highest energy and power density of 62.54 Wh $kg^{-1}$ and 42.307 kW $kg^{-1}$ [25]. This confirms that trimetallic positive electrode materials tend to present the highest power and energy density [25,28] generally assigned to properties such as large specific surface area, high porosity, and complex hollow sphere, yolk-shell and ball in ball structures. Those features can be enhanced by rational design and composition exploring the best of the individual constituents but also of synergistic effect of Ni, Co, Mn, V, Cu and other metal

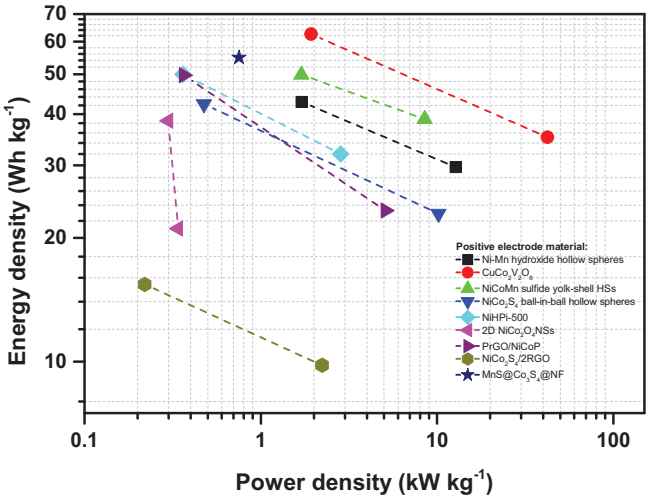


**Fig. 8.** Ragone plots for supercapacitor devices assembled with electrode materials prepared from metal-glycerolate precursors as positive electrodes. Only the highest power and energy density values of each electrode material are shown.

based materials [3,87,88]. Finally, it is important to emphasize that all electrodes to assemble devices are coated onto nickel foam (used as current collector) from a slurry or paste prepared by incorporating to the electrode materials, binders and additives such as polyvinylidene fluoride, isopropanol, acetylene black and *N*-methyl pyrrolidone. Accordingly, their relative amounts on the electrode influence the conductivity, mechanical properties, durability, and ultimately the performance of the energy storage device. In conclusion, metal-glycerolates provide an effective strategy for

preparation of high-performance electrode materials based on metal oxides, metal sulfides and metal phosphides, among others, with relatively complex structures, in a simple way making possible their large scale production and successful application in energy storage devices.

## 5. Metal-glycerolates and their derivatives for batteries

### 5.1. Metal-glycerolates and their derivatives as anode for LIBs

Electrode materials prepared from M−glycerolate precursors have wide application in metal ion batteries. In fact, as shown in Table 2, many mono- and bimetallic glycerolates were used in the design and preparation of different M−glycerolate derived materials, such as metal sulfides, metal phosphides, metal selenides and especially metal oxides.

Monometallic M−glycerolates were recently applied in lithium-ion batteries (LIBs) where excellent performances were reported. For example, one of the very promising results was reported by Ma *et al.* [90] who used 900 nm diameter $Fe_3O_4$ hollow spheres constructed from a large amount of radially standing 2D nanosheet precursor (~10 nm thick, Fig. 9**A-9C**), obtained by solvothermal annealing of Fe–glycerolate hollow spheres. The $Fe_3O_4$ hollow spheres exhibited initial discharge and charge capacities respectively of 1614 and 1063 mAh $g^{-1}$ (Coulombic efficiency (CE) of 66 %), and stable cycling performance over 100 discharge–charge cycles at a current density of 500 mA $g^{-1}$ (Fig. 9**D**). Good cyclability and charge retention capacity of 94 % in the second cycle was achieved after 100 cycles suggesting that $Fe_3O_4$ hollow spheres is a potential anode material of LIBs.

Other monometallic M−glycerolate derived materials were also reported for LIBs application such as $MoS_2$ [92] and Mo-PDA [93] (triple-shelled Mo-polydopamine). However, it is important to highlight that the construction of carbon-coated monometallic materials derived from M−glycerolate was recently reported as an interesting strategy for LIBs anode design. For instance, Wang and collaborators [91] reported a nickel phosphide nanoparticle assembled submicrospheres coated with a glucose-derived carbon shell ($Ni_2P$@C), prepared *via* calcination-phosphatization of a Ni-glycerolate precursor by carbon coating route (Fig. 9**E**). The $Ni_2P$@C electrode delivers a discharge and charge capacity respectively of 1514 and 1018 mAh $g^{-1}$ in the initial cycle, corresponding to a CE of 67 %. In addition, a high retention capacity of 587 mAh $g^{-1}$ after 400 cycles at 100 mA $g^{-1}$ was realized, demonstrating that the fabricated hybrid electrode exhibits better performance as LIBs anode than the $Ni_2P$ submicrospheres. According to the author, its unique core shell structure can naturally accommodate the volume change caused by (i) the progressive cycling and (ii) increase the electrical conductivity thus (iii) improving the kinetics of the electrochemical reaction at the $Ni_2P$ nanoparticles.

Similar strategy was used by Yuan *et al.* [23] who reported a universal chelation-carbonization-oxidation strategy to synthesize CoO nanocrystalline-assembled hierarchical mesoporous nanospheres starting from a Co-glycerolate precursor, followed by coating with $TiO_2$ and amorphous carbon (CoO@$TiO_2$@C, Fig. 9**F-9 J**). HMN CoO@$TiO_2$@C exhibited excellent lithium storage performance with the first discharge and charge capacities of 1538.8 and 1096.3 mAh $g^{-1}$, and CE of 71.2 %. The first three cycles at current density of 0.5 A $g^{-1}$ are shown in Fig. 9**K-9 M**, revealing that the carbon coating leads to the nearly overlapping of its discharge and charge profiles, indicating an excellent combined stabilizing effect of the $TiO_2$ and carbon coating. In fact, the robust $TiO_2$ and amorphous carbon shells improved the structural stability and electronic conductivity of CoO hierarchical mesoporous nanospheres [23].

Precursors based on bimetallic M−glycerolates have also been reported, especially for the development of metal oxide electrode materials such as $NiCo_2O_4$ hollow spheres [27], $NiCoO_2$ hollow submicrospheres [94] and $MnCo_2O_x$ [95]. It is important to mention that despite the data presented in Table 2, still there is much research to be done in the development of materials derived from bimetallic M−glycerolates. In addition, no work yet reported the preparation of trimetallic M−glycerolate derivatives, confirming that there is plenty of room for the development of new materials for batteries application. In fact, recent literature has shown that the development of bi- [3], tri- [87] and multimetallic and/or high-entropy [96] electrode materials is a new trend in the field of energy storage materials, especially the last ones.

In relation to bimetallic oxides derived from M−glycerolates, Shen *et al.* [27] and Wang *et al.* [94] reported the design and preparation of NiCo oxides with different phases from a similar NiCo-glycerolates precursor. More specifically, Shen *et al.* [27] synthesized a cubic spinel $NiCo_2O_4$ core-in-double-shell hollow spheres after a simple annealing of the precursor at 350 °C, in air, for 2 h, at a slow heating rate of 1 °C $min^{-1}$. The average diameters of the outer and inner shells as well as of the solid core was measured by TEM as being about 400, 200, and 40 nm, respectively. The $NiCo_2O_4$ electrode delivered a first-cycle discharge and charge capacity of 1401 and 928 mAh $g^{-1}$ respectively, corresponding to a CE of 66 %. Considering the previously reported discharge and charge capacities, the cubic spinel $NiCo_2O_4$ core-in-double-shell hollow spheres showed a greater capacity to store energy than the cubic crystallographic structure of $NiCoO_2$ hollow submicrospheres which shown the initial discharge and charge capacities of ~ 1034.8 and ~ 730.3 mAh $g^{-1}$, respectively, corresponding to a CE of ~ 70.5 % [94]. These results show that, even with no change in composition, structural modifications can provide relevant additional contribution to morphological changes, for the rational design of high-performance electrode materials.

### 5.2. Metal-glycerolates and their derivatives as anode for SIBs

The anode materials are far from satisfactory for development of competitive sodium-ion battery technologies [101] and yet a major scientific challenge. In this sense, M−glycerolates derived materials can play a major role since excellent results were reported when applied to the design and development of suitable anodes for SIBs, as shown in Table 2. More interestingly, in analogy to what was reported for LIBs, the preparation of carbon-coated M−glycerolates derived materials is a promising strategy for the design of electrode materials for SIBs. For instance, Zhang and coworkers [34] reported a hierarchical $MoSe_2$@C hollow nanospheres ($MoSe_2$@C HNSs), assembled with ultrathin nanosheets via a solvothermal method. Its fabrication involved an anion-exchange reaction from monometallic Mo-glycerolate solid spheres followed by a step of carbonization of glucose (Fig. 10**A-10C**). When used as an anode material for SIBs (Fig. 10**D**), the $MoSe_2$@C HNS composite performed gives a specific discharge capacity of 683.1 mAh $g^{-1}$ and charge capacity of 520.2 mAh $g^{-1}$ in the first cycle, with an initial CE of 76.2 % (Fig. 10**E**), and retained a capacity of 458 mAh $g^{-1}$ after 200 cycles at 200 mA $g^{-1}$. In fact, the performance of $MoSe_2$@C HNS electrode is relatively superior to the M−glycerolate derived hierarchical yolk-shell $MoSe_2$ spheres ($MoSe_2$ YSs) without carbon coating reported by Wang *et al.* [100] (Table 2). In this context, the excellent result must be evaluated considering other aspects than morphology. In fact, according to Zhang and coworkers [34] the synchronously incorporated carbon not only enhances the whole conductivity of $MoSe_2$@C HNS electrode material, but also acts as structural adhesives

**Table 2**
Comparison of the relevant electrochemical parameters of M−glycerolate derived materials and their performance in LIBs and SIBs.

| Type | Electrode Material | Electrode Material Morphology | Metal-Glycerate Precursor | Initial discharge (mAh $g^{-1}$) | Potential Window (V *vs* reference) | Reversible capacity (Nth) mAh $g^{-1}$ | % Stability (Cycles) | Ref. |
|---|---|---|---|---|---|---|---|---|
| Li-ion | $NiCoO_2$ | Hollow spheres | NiCo-glycerate | ~1034.8 | 0.01–3.0 V *vs* $Li/Li^+$ | ~709.0 (10) @ 100 mA $g^{-1}$ | ~119.2 % (750 at 0.5 A $g^{-1}$)<br>~72.9 % (750 at 2.0 A $g^{-1}$) | [94] |
| | α-MnS/$Co_9S_8$/C | Nanosheet-assembled flower-like morphology | MnCo-glycerate | 1376.2 | 0.01–3.0 V *vs* $Li/Li^+$ | 608 (300) @ 500 mA $g^{-1}$ | ~44.2 % (300 at 0.5 A $g^{-1}$) | [95] |
| | $MnCo_2O_x$ | Flower-like morphology | – | | 0.01–3.0 V *vs* $Li/Li^+$ | 203.4 (300) @ 500 mA $g^{-1}$ | 11.7 % (100 at 0.5 A $g^{-1}$) | |
| | $Fe_3O_4$ | Hollow spheres with ultrathin porous nanosheets | Fe–glycerate | 1614 | 0.01–3.0 V *vs* $Li/Li^+$ | 1046 (100) @ 500 mA $g^{-1}$ | 94 % (100 at 0.5 A $g^{-1}$)* | [90] |
| | $NiCo_2O_4$ | Core-in-double-shell hollow spheres | NiCo-glycerate | 1401 | 0.01–3.0 V *vs* $Li/Li^+$ | 885 (50) @ 150 mA $g^{-1}$ | 78 % (100 at 0.2 A $g^{-1}$)* | [27] |
| | Mo-PDA | Triple-shelled hollow spheres | Mo-glycerate | 1139 | 0.01–3.0 V *vs* $Li/Li^+$ | 580 (200) @ 500 mA $g^{-1}$ | –<br>(200 at 0.5 A $g^{-1}$) | [93] |
| | $MoS_2$ | Hollow nanospheres | Mo–glycerate | – | 0.01–3.0 V *vs* $Li/Li^+$ | 1100 (100) @ 500 mA $g^{-1}$ | 86.6 % (100 at 0.5 A $g^{-1}$)* | [92] |
| | HMN CoO@$TiO_2$@C | CoO hierarchical mesoporous nanospheres coated by $TiO_2$ and amorphous carbon | Co-glycerate | 1538.8 | 0.01–3.0 V *vs* $Li/Li^+$ | 1136 (200) @ 500 mA $g^{-1}$ | ~73.8 %(200 at 0.5 A $g^{-1}$) | [23] |
| | $Ni_2P$@C | Submicrospheres | Ni-glycerate | 1514 | 0.0–3.0 V *vs* $Li/Li^+$ | 587 (400) @ 100 mA $g^{-1}$ | –<br>(400 at 0.1 A $g^{-1}$) | [91] |
| | $MoSe_2$@C | Hollow nanospheres | Mo-glycerate | 1005 | 0.0–3.0 V *vs* $Li/Li^+$ | 711 (300) @ 500 mA $g^{-1}$ | 98 % (300 at 0.5 A $g^{-1}$)** | [34] |
| | HYIFs | Hollow yolk-like spheres | Fe-glycerate | 306 | 1.5–4.2 V *vs* $Li/Li^+$ | 220 (25) @ 71.2 mA $g^{-1}$ | ~53.6 % (40 at 0.0712 A $g^{-1}$) | [97] |
| Na-Ion | $(Ni_{0.33}Co_{0.67})_9S_8$@C nanospheres. | Ball-In-Ball Structured with the free hollow space and complete carbon layer | NiCo-glycerate | – | 0.01–3.0 V *vs* $Na/Na^+$ | 335.1 (200) @ 1000 mA $g^{-1}$ | – | [98] |
| | $(Ni_{0.33}Co_{0.67})_9S_8$/C mixture | Ball-In-Ball Structured | | – | 0.01–3.0 V *vs* $Na/Na^+$ | 23.4 (200) @ 1000 mA $g^{-1}$ | – | |
| | $NiCo_2O_4$ | Double-shelled hollow spheres | NiCo DH-glycerol composites | 814 | 0.01–3.0 V *vs* $Na/Na^+$ | 341 (100) @ 100 mA $g^{-1}$ | 66 % (100 at 0.1 A $g^{-1}$)* | [99] |
| | $MoSe_2$ | Yolk-shell spheres | Mo–glycerate | 542.1 | 0.01–3.0 V *vs* $Na/Na^+$ | 335.9 (100) @ 200 mA $g^{-1}$ | ~62 % (100 at 0.2 A $g^{-1}$)* | [100] |
| | $Ni_2P$@C submicrospheres | Submicrospheres coated by a continuous carbon coating shell | Ni-glycerate | 714 | 0.0–3.0 V *vs* $Na/Na^+$ | 296 (100) @ 50 mA $g^{-1}$ | –<br>(100 at 0.05 A $g^{-1}$)* | [91] |
| | $MoSe_2$@C | Hollow nanospheres | Mo-glycerate | 683 | 0.01–3.0 V *vs* $Na/Na^+$ | 458 (200) @ 200 mA $g^{-1}$ | ~75.4 % (200 at 0.2 A $g^{-1}$) | [34] |
| | $V_2S_3 \subset C$ | Hollow spheres with a core–shell structure | V-glycerate | 850 | 0.01–3.0 V *vs* $Na/Na^+$ | 777 (-) @ 100 mA $g^{-1}$ | ~100 % (600 at 1.5 A $g^{-1}$) | [101] |
| | Y-$CoMoO_xS_y$ | Yolk–shell spheres | CoMo-glycerate | 692.2 | 0.01–3.0 V *vs* $Na/Na^+$ | 479.4 (100) @ 200 mA $g^{-1}$ | ~69.2 (100 at 0.2 A $g^{-1}$) | [102] |
| | Y-$CoMoO_4$ | Yolk–shell spheres | | – | 0.01–3.0 V *vs* $Na/Na^+$ | 26.9 (100) @ 200 mA $g^{-1}$ | -<br>(100 at 0.2 A $g^{-1}$) | |
| | H-$CoMoO_xS_y$ | Hollow spheres | | – | 0.01–3.0 V *vs* $Na/Na^+$ | 227.7 (100) @ 200 mA $g^{-1}$ | -<br>(100 at 0.2 A $g^{-1}$) | |

NiCo DH = Ni–Co double hydroxide, Mo-PDA = triple-shelled Mo-polydopamine, * = from the second cycle onward. ** = in terms of charge capacity. HYIFs = hollow yolk-like spheres iron fluoride, SSIFs = single solid spheres iron fluoride.

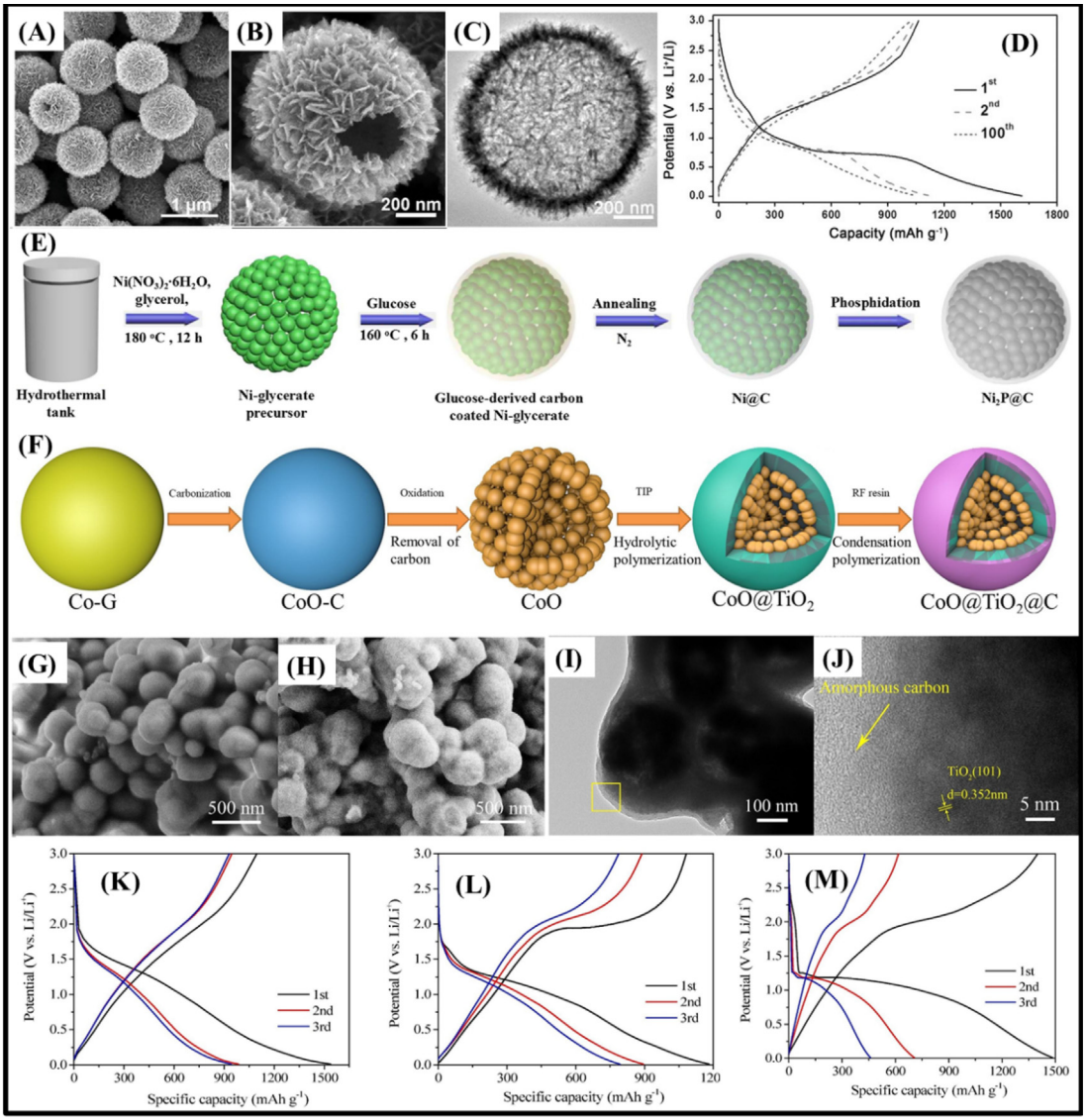


**Fig. 9.** (A-B) FESEM images and (C) TEM image of as-prepared hierarchical $Fe_3O_4$ hollow spheres. (D) charge–discharge voltage profiles for the first, second, and 100th cycles at a constant current density of 500 mA $g^{-1}$. Reproduced with permission from ref. [90]. Copyright © 2015 WILEY-VCH Verlag GmbH & Co. KGaA, Weinheim. (E) Schematic illustration of the synthetic process of $Ni_2P$@C submicrospheres. Reproduced with permission from ref. [91]. Copyright © 2018 Elsevier Inc. All rights reserved. (F) Schematic illustration of the HMN CoO@$TiO_2$@C synthesis. (G) SEM image of HMN CoO@$TiO_2$; and (H) SEM, (I) TEM and (J) HRTEM images of HMN CoO@$TiO_2$@C. Galvanostatic discharge–charge profiles of the first three cycles of (K) HMN CoO@$TiO_2$@C, (L) HMN CoO@$TiO_2$ and (M) HMN CoO, at a current density of 0.5 A $g^{-1}$. Reproduced with permission from ref. [23]. Copyright © 2021 Elsevier B.V. All rights reserved.

contributing to the maintenance of structural integrity during charging/discharging processes [34].

In addition to selenides, even better results were reported when monometallic M−glycerolates were also used as precursors in the preparation of carbon-coated metal sulfides ($V_2S_3$ ⊂ C [101]) and phosphides ($Ni_2P$@C [91]). For example, Shen *et al.* [101] developed a hierarchical nanoscale carbon coated vanadium sulfide ($V_2S_3$ ⊂ C) spheres with a core–shell structure based on a simple thermal sulfurization (Fig. 10**F-10G**), which delivers discharge and charge capacities of 850 and 777 mAh $g^{-1}$ during the first cycle, respectively, with a high CE of 91.4 % (Fig. 10***H***). In addition, the $V_2S_3$ ⊂ C material exhibited a highly reversibly sodium storage capacity of 777 mAh $g^{-1}$ at 100 mA $g^{-1}$, excellent rate capability of 410 mAh $g^{-1}$ at 4000 mA $g^{-1}$, and impressive cycling ability. According to the authors, the design strategy based on an efficient electron/ion conducting network, can overcome the problems associated with the energy conversion reactions and may inspire the design of a wide range of high-performance electrode materials [101] (Fig. 10**I-10 J**).

In addition to monometallic materials, bimetallic M−glycerolates based sulfides have also been recently reported. In fact, metal sulfides has been considered a class of highly promising electrode materials for energy storage and conversion, especially when they present core–shell [86] or yolk–shell [103] structures, due to the unique cavity structure between the yolk and the shell, which can accommodate the volume changes during charge–discharge, thus alleviating the mechanical stress on the electrode [102]. In this context, Wang *et al.* [102] reported the fabrication of amorphous yolk–shell Co-Mo oxide/sulfide nan, spheres (Y-$CoMoO_xS_y$) via solvothermal sulfurization of CoMo-glycerolate using thioacetamide as sulfur source (Fig. 11**A**). The electrochemical performance of Y-$CoMoO_xS_y$ was compared with those of Y-$CoMoO_4$ and H-$CoMoO_xS_y$ electrodes. According to the authors, the superior sodium storage performance of the Y-$CoMoO_xS_y$ electrode in terms

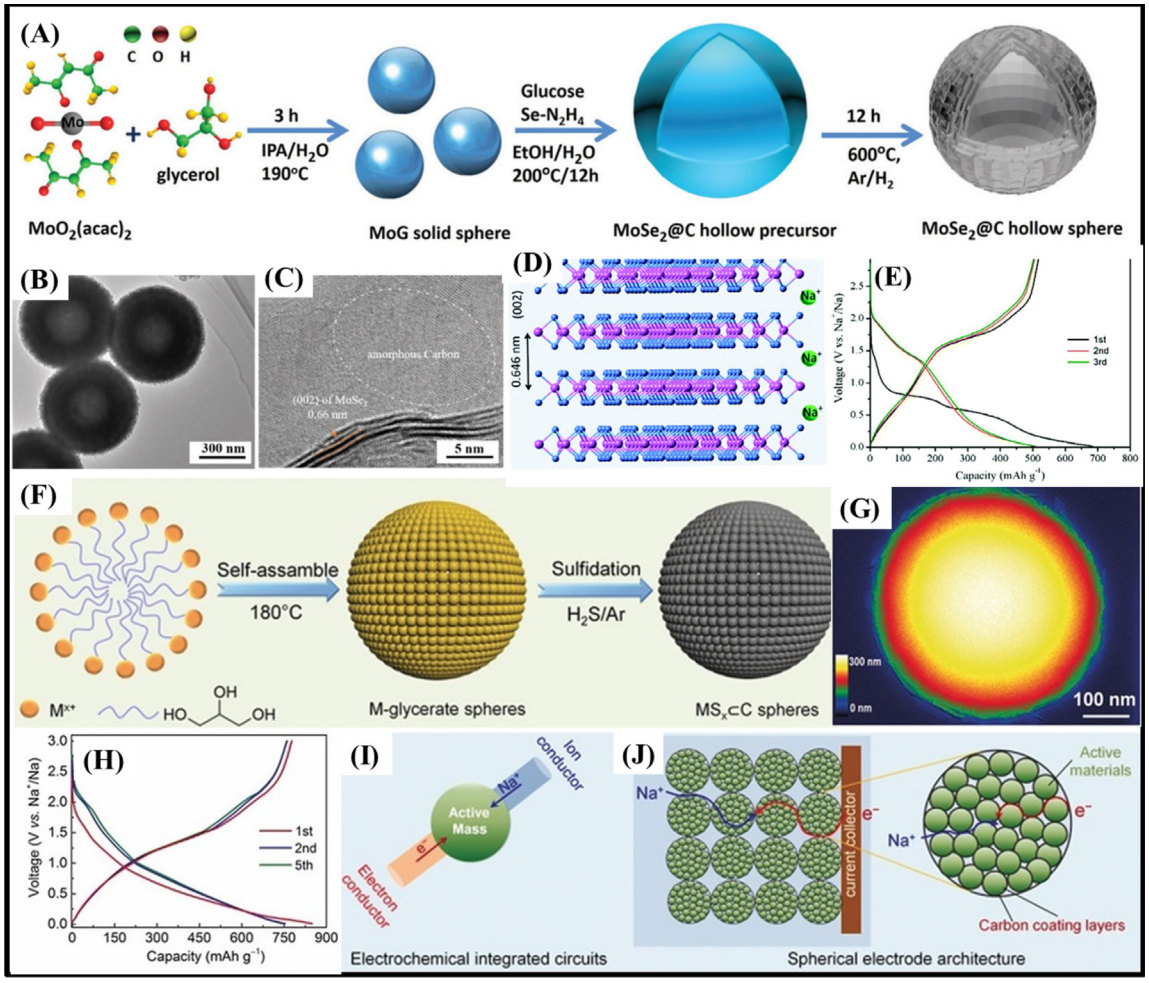


**Fig. 10.** (A) Schematic illustration of the synthesis of hierarchical $MoSe_2$@C hollow nanospheres. (B) TEM and (C) HRTEM image of $MoSe_2$@C HNS. (D) Structure model of layered $MoSe_2$; (E) Electrochemical performance of $MoSe_2$@C HNSs as anode materials for SIBs showing the discharge–charge voltage profiles at a current density of 100 mA $g^{-1}$. Reproduced with permission from ref. [34]. Copyright © the Partner Organisations 2020. (F) Schematic illustration of the formation process and (G) EFTEM thickness mapping of hierarchical $MS_x \subset C$ spheres. (H) Electrochemical performance of the $V_2S_3 \subset C$ spheres showing the discharge–charge voltage profiles for the first, second, and fifth cycle at a current density of 100 mA $g^{-1}$. Schematic diagrams of (I) electrochemically integrated circuit employing ionic and electronic conductors and (J) the active mass and spherical hierarchical architecture of the electrode material. Reproduced with permission from ref. [101]. Copyright © 2019 Wiley-VCH Verlag GmbH & Co. KGaA, Weinheim.

of specific capacity, cycling stability, and rate capacity was assigned to the synergistic enhancement effects provided by the unique yolk–shell nanosphere architecture and the amorphous Co/Mo oxides/sulfides. In fact, the number of electrochemically active sites for intercalation of sodium ions was increased by the inner yolk of the yolk–shell nanospheres enhancing the energy density. In addition, the pulverization of electrodes was suppressed by the middle cavity between the yolk and the shell, preventing the volume change of electrodes during the charge and discharge processes. In addition, the amorphous structure has a very important role since it provides multiple $Na^+$ diffusion pathways and more electrochemically active sites for $Na^+$ intercalation, thus making it possible to anticipate the preparation of advanced electrode materials for electrochemical energy storage in near future.

## 6. Metal-glycerolates and their derivatives for water-splitting

### *6.1. Metal-glycerolates and their derivatives as electrocatalyst materials for HER*

Hydrogen evolution reaction is a multi-step two electron transfer process that occurs at the electrode surface [104,105] in acidic and alkaline medium. A good catalyst for HER must have a hydrogen adsorption free energy ($\Delta G_H^*$) close to zero. This energy is related to the ease of breaking bonds between hydrogen and the catalyst surface. Good catalysts such as the Pt-based materials, show weak interactions assuring a fast release of hydrogen from the surface. Weak interactions mean low free energy of hydrogen adsorption [104]. Platinum-derived materials are known to be efficient HER catalysts but its scarcity on earth and consequent high cost decrease the competitiveness. Accordingly, it is necessary to study and develop noble metal-free electrocatalysts with similar efficiency, robustness, stability, and low associated cost to increase the possibility of industrial use [106,107].

Metal-glycerolates can be used as template for preparation of different types of electrocatalysts, where Co [108,109] and NiCo-containing phosphide [110,111] have been predominantly developed and gained considerable interest as potential electrocatalysts for HER (Table 3).

For instance, Guo and co-workers [109] synthesized monometallic hierarchical cobalt phosphide (CoP) nanospheres using solid cobalt-glycerolate (CoG) nanospheres as a sacrificial template. The CoG was prepared by a two-step solvothermal process and, after phosphorization reaction, converted into hierarchi-

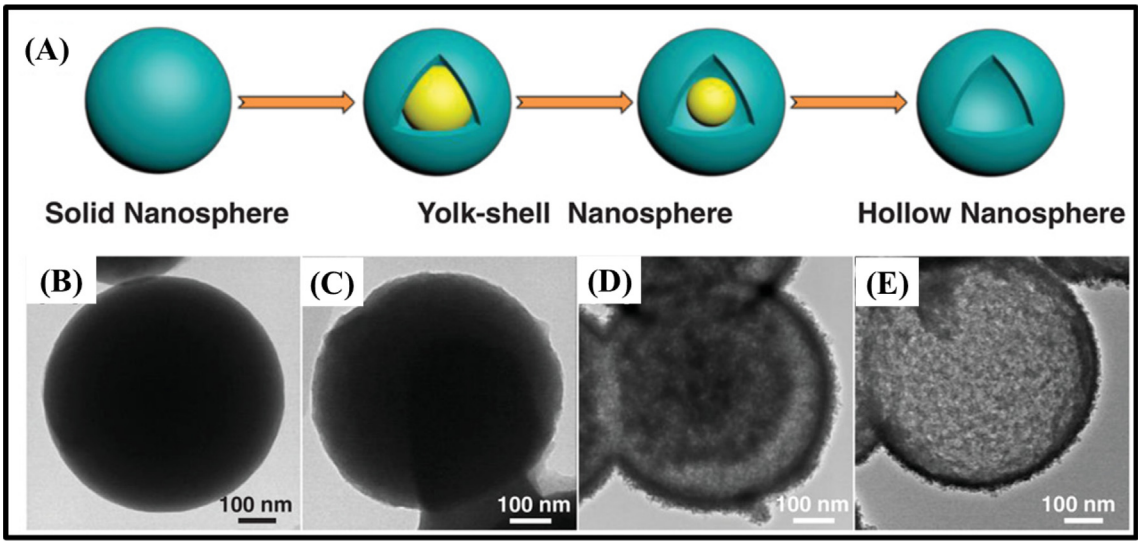


**Fig. 11.** (A) Schematic illustration of the evolutions from solid CoMo-glycerolate nanospheres to yolk–shell and hollow $CoMoO_xS_y$ nanospheres. TEM images for (B) CoMo-glycerolate and the resulting products after solvothermal sulfurization with thioacetamide for increasing reaction times: (C) 0.5 h, (D) 2 h, (E) 6 h. Reproduced with permission from ref. [102]. Copyright © 2020 WILEY-VCH Verlag GmbH & Co. KGaA, Weinheim.

**Table 3**
Performance parameters of recently reported M−glycerolates and their derivatives electrocatalysts for HER/OER: overpotential at 10 mA $cm^{-2}$, onset potential, Tafel slope, and stability.

| | Catalyst | Precursors | Preparation Method | Substrate | $\eta_{10}$(mV) | Tafel Slope (mV $dec^{-1}$) | Stability (h) | pH condition | Ref. |
|---|---|---|---|---|---|---|---|---|---|
| **OER** | Mn-Co-P YS | Co-glycerolate | Solvothermal/Phosphorization | GCE | 330 | 59 | 8 | 1.0 M KOH | [117] |
| | CoCuFe-Gly | CoCu-glycerolate | Solvothermal | GCE | 317 | 69 | 8 | 1.0 M KOH | [11] |
| | 5TMZ | CrMnFeCoNi-glycerolate | Solvothermal | Ni foam | 251* | 42.3 | 60 | 1.0 M KOH | [118] |
| | Fe-$Co_xP$ | Co-glycerolate | Solvothermal/Phosphorization | GCE | 300 | 49 | 12 | 1.0 M KOH | [119] |
| | CoOOH | Co-glycerolate | Solvothermal/ | Ni foam | 275 | 49 | 12 | 1.0 M KOH | [120] |
| | NiCo-HP | NiCo-glycerolate | Solvothermal | CPE | 320 | 84 | 15 | 1.0 M KOH | [121] |
| | NiCoCrMn-G | NiCoCrMn-glycerolate | Solvothermal | Ni foam | 229 | 40 | 36 | 1.0 M KOH | [122] |
| | Ni-Co-TEP | NiCo-glycerolate | Solvothermal/Calcination | GCE | 310 | 68 | 16 | 1.0 M KOH | [123] |
| | CoP/$C_{PDS}$ | Co-glycerolate | Solvothermal/Carbonization/ Phosphorization | Ni foam | 280 | 144 | 15 | 1.0 M KOH | [108] |
| | FeNiGly | FeNi-glycerolate | Solvothermal | GCE | 320 | 50 | 25 | 1.0 M KOH | [18] |
| | NiCo-Fe LDH | NiCo-glycerolate | Solvothermal/Hydrothermal | GCE | 285 | 62 | 12 | 1.0 M KOH | [124] |
| | CoFeG-HS | CoFeG-HS | Solvothermal | GCE | 242.0 | 49.4 | 50 | 1.0 M KOH | [125] |
| **HER** | CoP | Co-glycerolate | Solvothermal/Phosphorization | GCE | 121 | 56 | 1000 cycles | 0.5 M $H_2SO_4$ | [109] |
| | NiCoP | NiCo-glycerolate | Solvothermal/Phosphorization | GCE | 95<br>127 | 63<br>61 | 24 | 0.5 M $H_2SO_4$<br>1.0 M KOH | [111] |
| | CoP/$C_{PDS}$ | Co-glycerolate | Solvothermal/Carbonization/ Phosphorization | Ni foam | 101 | 79 | 15 | 1.0 M KOH | [108] |
| | NiCoP-H | NiCo-glycerolate | Hydrothermal/Solvothermal | GCE | 90<br>121<br>157 | 68<br>65<br>84 | 24 | 0.5 M $H_2SO_4$<br>1.0 M KOH<br>0.5 M PBS | [110] |

$C_{PDS}$ = P-doped Dual Carbon Shells; CPE = Carbon Paper Electrode; GCE = Glass Carbon Electrode; Gly, G = Glycerolate; H = Hollow; HP = Hydrogen Phosphate; HS = Hollow Sphere; LDH = Layered Double Hydroxide; P = Phosphide; PBS = Phosphate Buffered Saline; TEP = Triethyl Phosphate; YS = Yolk-shell; 5TMZ = CrMnFeCoNiTiZn-glycerolate; 5 M = CrMnFeCoNi-glycerolate.
*=$\eta_{50}$(50 mA $cm^{-2}$).

cal CoP nanospheres with well-preserved morphology. Under acidic condition (0.5 M $H_2SO_4$), it exhibited an overpotential of 121 mV at a current density of 10 mA $cm^{-2}$, a low Tafel slope of 56 mV and similar performance up to 1000 voltammetric cycles. The good result was attributed to the hierarchical structures capable of reducing mass transfer resistances, improving electrolyte penetration and diffusion, since the best catalytic performance was presented by nanospheres with ultrathin nanosheet subunits [109].

Acidic electrolytes (e.g., $H_2SO_4$) provide a high concentration of protons that are used during the HER process, thus being one of the most used conditions to evaluate the electrocatalytic activity of

electrocatalytic materials. However, a corrosive acidic fog is generally formed under such conditions, contaminating the $H_2$ gas produced and corroding the electrocatalysts. Thus, expensive anion exchange membranes, as well as electrocatalysts, [112] resistant to acidic conditions and with minimum gas crossover, are required under industrial conditions.

Fortunately, materials resistant to both conditions have been developed. For instance, Liu and co-workers [111] reported the preparation of a bimetallic hierarchical nickel–cobalt phosphide (NiCoP) hollow nanoflowers with ultrathin nanosheet assembly, by hydrothermal treatment of solid NiCo-glycerolate nanospheres followed by phosphorization. In alkaline medium (1 M KOH), NiCoP exhibited an overpotential of 127 mV at a current density of 10 mA $cm^{-2}$ and Tafel slope of 61 mV. Electrochemical evaluations under acidic conditions (0.5 M $H_2SO_4$) showed an overpotential of 95 mV at a current density of 10 mA $cm^{-2}$ and Tafel slope of 63 mV. In both conditions, the material showed stability for at least 24 h. Compared with solid NiCoP nanospheres, the hollow NiCoP nanoflowers with ultrathin nanosheets is a more efficient HER electrocatalyst due to high specific surface area, generating large exposed active sites and affluent mass diffusion routes [111].

In the same line but in a more complete research that evaluated the electrocatalytic activity under acidic, neutral and alkaline conditions, Liu *et al.* [110] synthesized via solvothermal process a bimetallic nickel – cobalt phosphide (Ni-Co—P—H) hollow nanoflowers with ultrathin nanosheet arrays (Fig. 12**A-12D**) using NiCo-Glycerolate as a template. Under acidic conditions (0.5 M $H_2SO_4$) the material exhibited an overpotential of 90 mV at a current density of 10 mA $cm^{-2}$ and Tafel slope of 68 mV (Fig. 12**E-12G**). Under neutral conditions (0.5 M PBS) the overpotential increased to 157 mV at a current density of 10 mA $cm^{-2}$ and Tafel slope to 84 mV (Fig. 12**H-12 J**). Finally, in 1 M KOH the overpotential receded to 121 mV at a current density of 10 mA $cm^{-2}$ and Tafel slope of 65 mV (Fig. 12**K-12 M**). This electrocatalyst was stable for 24 h under all pH conditions analyzed. The ultrathin nanosheets are favored by the abundance of active sites. The porous core–shell structure, on the other hand, in addition to preventing the aggregation of nanosheets, generates channels for efficient mass transfer, increasing the catalytic activity for HER. Furthermore, the incorporation of Ni into CoP to form CoP/NiCoP optimized the electronic structure and boosted its electrocatalytic activity (**Image 12 N-12P**) [110].

To perform the overall water splitting, Mohite and co-workers [108] prepared P-doped dual carbon shells coated with cobalt phosphide nanoparticles ($CoP/C_{PDS}$), using a Co-glycerolate precursor obtained via solvothermal process. Electrocatalytic evaluations for HER, under alkaline conditions, showed an overpotential of 101 mV at a current density of 10 mA $cm^{-2}$ and Tafel slope of 79 mV. The OER tests resulted in an overpotential of 280 mV at a current density of 10 mA $cm^{-2}$ and Tafel slope of 144 mV. Interestingly, the material showed a durability of 15 h in both conditions but a comparison with the others reported here demonstrated that it does not perform as well. For example, its Tafel slope, both in OER and HER, were much higher indicating a slower reaction kinetics. However, any other material reported so far is as versatile as $CoP/C_{PDS}$ working as a bifunctional electrocatalyst.

### 6.2. Metal-glycerolates and their derivatives as photocatalyst materials for HER

The use of solar energy to carry out the water splitting over semiconductor photocatalysts is an alternative [113]. In this context, transition metal chalcogenides have been used as an promising alternative to improve the photocatalytic capacity of wide bandgap semiconductor materials [114]. For example, Huang and co-workers [115] prepared the metal compound Ni-glycerolate and combined it with chalcogenide-based compound $Zn_{0.5}Cd_{0.5}S$, to form the nanocomposites $Zn_{0.5}Cd_{0.5}S$@Ni-glycerolate with a core–shell structure. Under photocatalytic conditions, the material showed $H_2$ production rate up to 2800 μmol $h^{-1}$ 0.1 $g^{-1}$, about 6 times that of pure $Zn_{0.5}Cd_{0.5}S$. In this case, the metal glycerolate helps in the separation of the photoinduced charges and accelerates the photocatalytic water decomposition reaction. Using a similar material, Gholipour *et al.* [116] synthesized zinc cadmium sulfide ($Zn_xCd_{1-x}S$) by utilizing metal-glycerolate followed by calcination in air and sulfuration under flowing $H_2S$. Changing the Zn/Cd ratio, the researchers evaluated the material's photocatalytic capacity. Under a solar simulator, the best result was obtained with the $Zn_{30}Cd_{70}S$ material that exhibited a hydrogen evolution of 12 mmol $h^{-1}$ $g^{-1}$. These recent works demonstrate the potential of M−glycerolate based materials as photocatalysts for HER, and there is still much unexplored space for these applications.

### 6.3. Metal-glycerolates and their derivatives as electrocatalyst materials for OER

As an alternative to the noble metals commonly used as OER electrocatalyst, significant advances were achieved with the first transition series elements such as Mn, Fe, Ni and Co, generally as nitrides [126], phosphates [121,123], phosphides [127], oxides [128,129], hydroxides [5,130,131] and hybrid materials [132], exploiting the synergy of different transition metals [133].

In this regard, metal-glycerolates can be a powerful electrocatalyst and a template for obtaining other types of catalytic materials. In fact, since 2019, research involving glycerolates has demonstrated the possibility of developing durable and efficient OER electrocatalytic materials based on earth abundant metals such as Ni and Co. In fact, cobalt is present in 10 of the 11 materials reported here. Moreover, phosphorus containing electrocatalytic compounds, such as metal phosphides and phosphates, are being more commonly used than other derivatives, due to their good electrochemical activity and high conductivity [121,134]. For instance, the open structure framework, rich redox behavior and the relatively strong P—O covalent bonds in the structure of metal phosphates make them promising materials for electrochemistry [134]. However, analyses carried out after the OER experiments proved that, in most of these cases, the active species ends up being converted to the respective oxyhydroxide. Similar to metal phosphates, it is important to highlight that despite the good stability of metal phosphides for HER, under anodic oxidation reaction conditions, this class of materials is also being transformed *in situ* into their corresponding high activity oxyhydroxides [127]. This behavior was observed in both, metal phosphates and phosphides prepared from metal-glycerolates, showing that the OER active site probably is the respective metal oxyhydroxide.

In fact, Septiani and co-workers [121] monitored *in situ* by XPS analysis the transformation of a bimetallic nickel–cobalt (Ni-Co) hydrogen phosphate nanotubes (NiCo-HP) into active Ni-Co oxyhydroxide species on the surface of the NiCo-HP electrode after OER. The material was prepared using monodispersed NiCo-glycerolate spheres, previously obtained by a solvothermal method, as self-sacrificial templates. The best OER electrocatalytic activity was achieved with the material with the highest Ni/Co ratio, that presented a Tafel slope of 84 mV $dec^{-1}$ and an overpotential of 320 mV at a current density of 10 mA $cm^{-2}$. The authors attributed this result to its lower charge transfer resistance, increased density of active sites and the nanotube-assembled 2D architectures providing enhanced interconnectivity between the particles to create a highly conductive network for diffusion of electrolyte ions [121].

In addition, Septiani and co-workers [123] used NiCo-glycerolate as the precursor (Fig. 13**B**) and triethyl phosphate (TEP) to induce the self-assembly of uniform Ni – Co phosphate

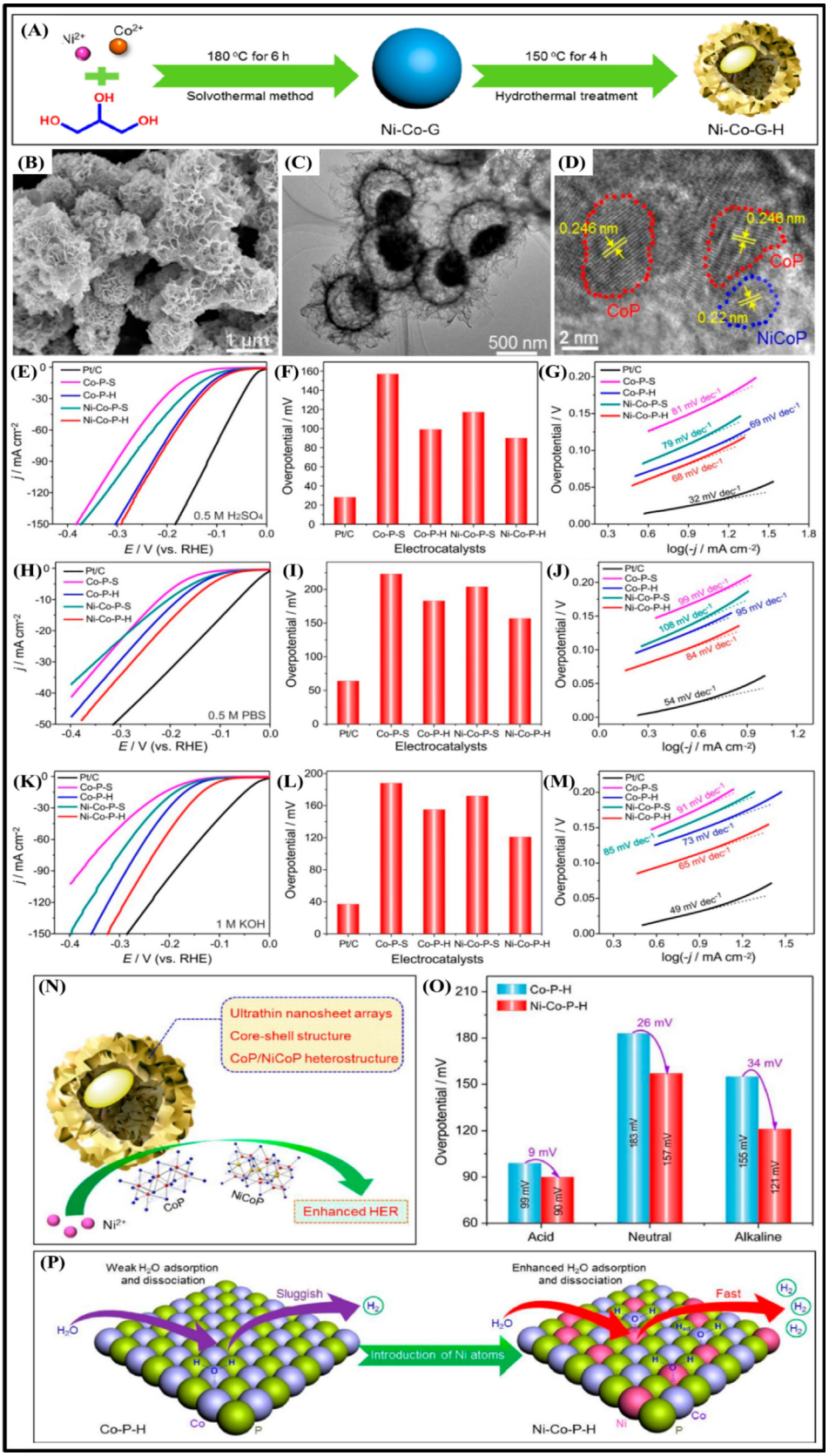


**Fig. 12.** (A) Schematic illustration of the synthesis of the Ni-Co—P—H microflowers with ultrathin nanosheet arrays. (B) SEM image, (C) TEM image and high-resolution TEM image of Ni-Co—P—H. In 0.5 M $H_2SO_4$: (E) Polarization curves of Pt/C, Co – P — S, Co – P — H, Ni – Co – P — S, and Ni – Co – P — H, (F) Overpotentials and (G) Tafel plots. In 0.5 M PBS: (H) Polarization curves, (I) Overpotentials and (J) Tafel plots. In 1 M KOH: (K) Polarization curves, (L) Overpotentials and (M) Tafel plots. (N) Ni –Co—P—H system diagram. (O) Comparison of the overpotentials between Co – P — H and Ni – Co – P — H in 0.5 M $H_2SO_4$, 0.5 M PBS, and 1 M KOH solutions. (P) Schematic diagram of improved HER performance at alkaline and neutral conditions due to the enhanced adsorption and dissociation of $H_2O$ molecules by introduction of Ni atoms. Reproduced with permission from ref. [110]. Copyright © 2019 American Chemical Society.

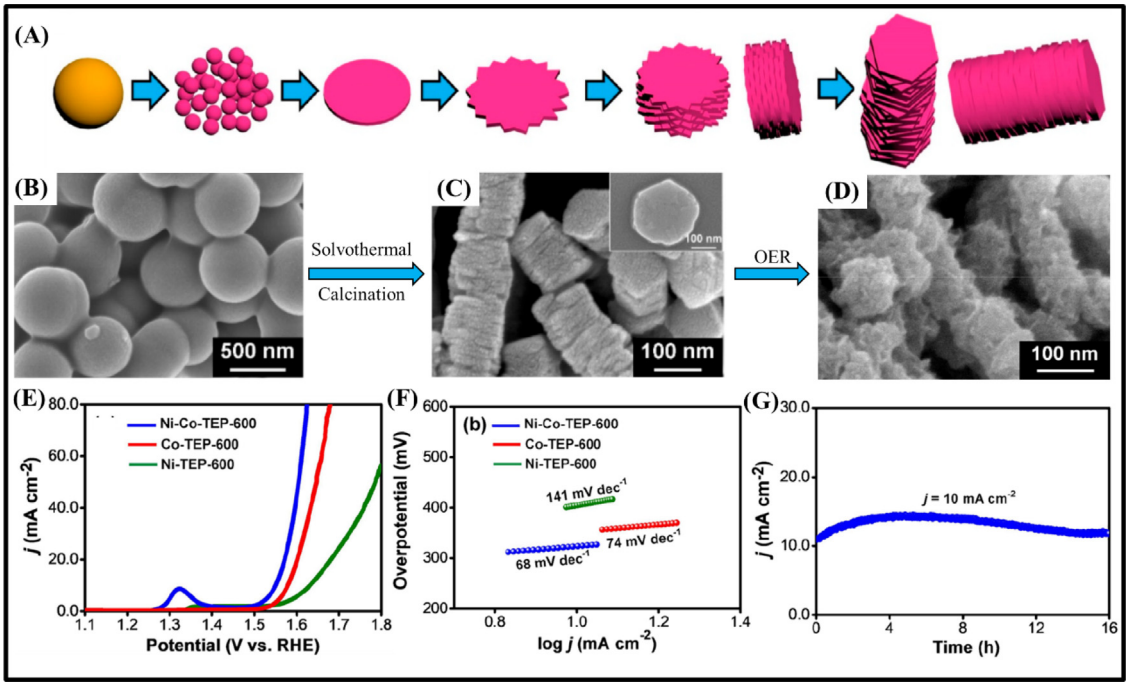


**Fig. 13.** (A) Schematic illustration of the catalyst formation process from the NiCo-glycerolate precursor. (B) SEM image of Co-Ni-Glycerolate. (C) SEM image of Ni-Co-TEP after the synthesis process. (D) SEM image of the catalyst post OER process. (E) Polarization curves, Tafel plots (F) and stability test of Ni-Co-TEP. Reproduced with permission from ref. [123]. Copyright © 2020 American Chemical Society.

nanoplates into porous 1D chainlike particles (Ni-Co-TEP) (Fig. 13**C**), upon a solvothermal and calcination process (Fig. 13**A**). The bimetallic glycerolate is essential for generating ethyl glycerolate during the solvothermal reaction, which is responsible for the self-stacking of these nanoplates into chainlike structures. The electrochemical measurements (Fig. 13**E-13G**) indicated an OER overpotential of 310 mV at a current density of 10 mA $cm^{-2}$ and Tafel slope of 68 mV $dec^{-1}$. Furthermore, the bimetallic phosphate catalyst exhibited electrochemical stability even after 16 h of continuous electrolysis. The XPS measurements of Ni-Co-TEP post OER process exhibited the oxidation of the $Ni^{2+}$/$Co^{2+}$ to the corresponding $Ni^{3+}$/$Co^{3+}$ species, indicating that the actual catalytic sites may originate during the conversion of the phosphate derivative to the Ni – Co oxyhydroxide, where the Ni cations synergistically enhance the catalytic activity. The presence of phosphate in the system can help in the activity of the electrocatalyst since it may distort the nickel or cobalt coordination geometry, increasing the stability of the activated complex by Jahn – Teller effect while enhancing the electronic interactions between Ni-Co and the oxygen atoms. Post-OER SEM images of the material (Fig. 13**D**) showed the presence of sheetlike structures on the surface, attributed to the formation of the metal oxyhydroxide phase [123].

Kaneti and co-workers [117] synthesized manganese-cobalt phosphide yolk-shell spheres (Mn-Co-P YS) (Fig. 14**A-14C**) instead of bimetallic phosphates by mixed hydrothermal solvothermal reaction of cobalt glycerolate spheres, as a sacrificial template. This material exhibited an overpotential of 330 mV at a current density of 10 mA $cm^{-2}$, a Tafel slope of 59.0 mV $dec^{-1}$ and 8 h stability, presenting superior results as compared to the analogous Mn-Co oxide yolk-shell spheres and the monometallic cobalt phosphide (Fig. 14**J and 14 K**). Analogously to the previously discussed metal phosphate derivatives, the post-OER analysis by XPS indicated the formation of $Mn^{4+}$/$Mn^{3+}$ and $Co^{3+}$/$Co^{2+}$ oxyhydroxide species on the surface which may be responsible for the electrocatalytic activity (Fig. 14**D-14I**). The presence of metal ions such as Mn in different valence states ($Mn^{3+}$ and $Mn^{2+}$) suggest the formation of a mixed valence material with higher conductivity and much faster electron transfer via the polaron hopping conduction mechanism, increasing the catalytic activity. Furthermore, the presence of the two redox couples of Mn and Co may be able to provide donor–acceptor chemisorption sites for the reversible adsorption/desorption of oxygen, assisting the OER [117].

The best result of a phosphorus compound electrocatalyst was obtained by Song and co-workers [119] with the Fe-$Co_x$P hollow iron cobalt phosphide. Co-glycerolate nanospheres (Fig. 15**A**), synthesized by a solvothermal process, were used as sacrificial templates. The hollow Fe-$Co_x$P nanospheres were obtained after anion-exchange and phosphorization process (Figure 145-15**D**). The catalyst showed excellent activity for OER when compared to other previously reported materials, exhibiting an overpotential of 300 mV at a current density of 10 mA $cm^{-2}$ (Fig. 15**E**), and Tafel slope of 49 mV $dec^{-1}$ (Fig. 15**F**), indicating a favorable electrocatalytic kinetics for OER. In addition, the chronoamperometry test has proven catalyst stability for at least 12 h (Fig. 15**G**). In this case also, there was the formation of FeCo (oxy)hydroxides in the surface, as confirmed by post-OER XPS analysis. The good catalytic activity was attributed to (a) the morphology of the catalyst, where the Fe-$Co_x$P core can serve as a conductive support for rapid electron transfer, enhancing the synergistic effect between the oxo/hydroxo surface species, active for the OER, and the intrinsic metal phosphide; (b) the high hydrophilicity and surface roughness contributing to enhance the OER performance in alkaline solution; (c) the synergistic effect on bimetallic system and (d) enhanced surface area and density of active sites due to the hollow structure [119].

In addition to phosphides and phosphates, transition metal-based hydroxides/oxyhydroxide are known as promising alternatives to noble metal-based electrocatalyst [77,130]. For instance, Wang and co-workers [120] report the synthesis of hierarchical ultrathin sheet-based CoOOH hollow nanospheres, using Co-glycerolate as a precursor synthesized by solvothermal process.

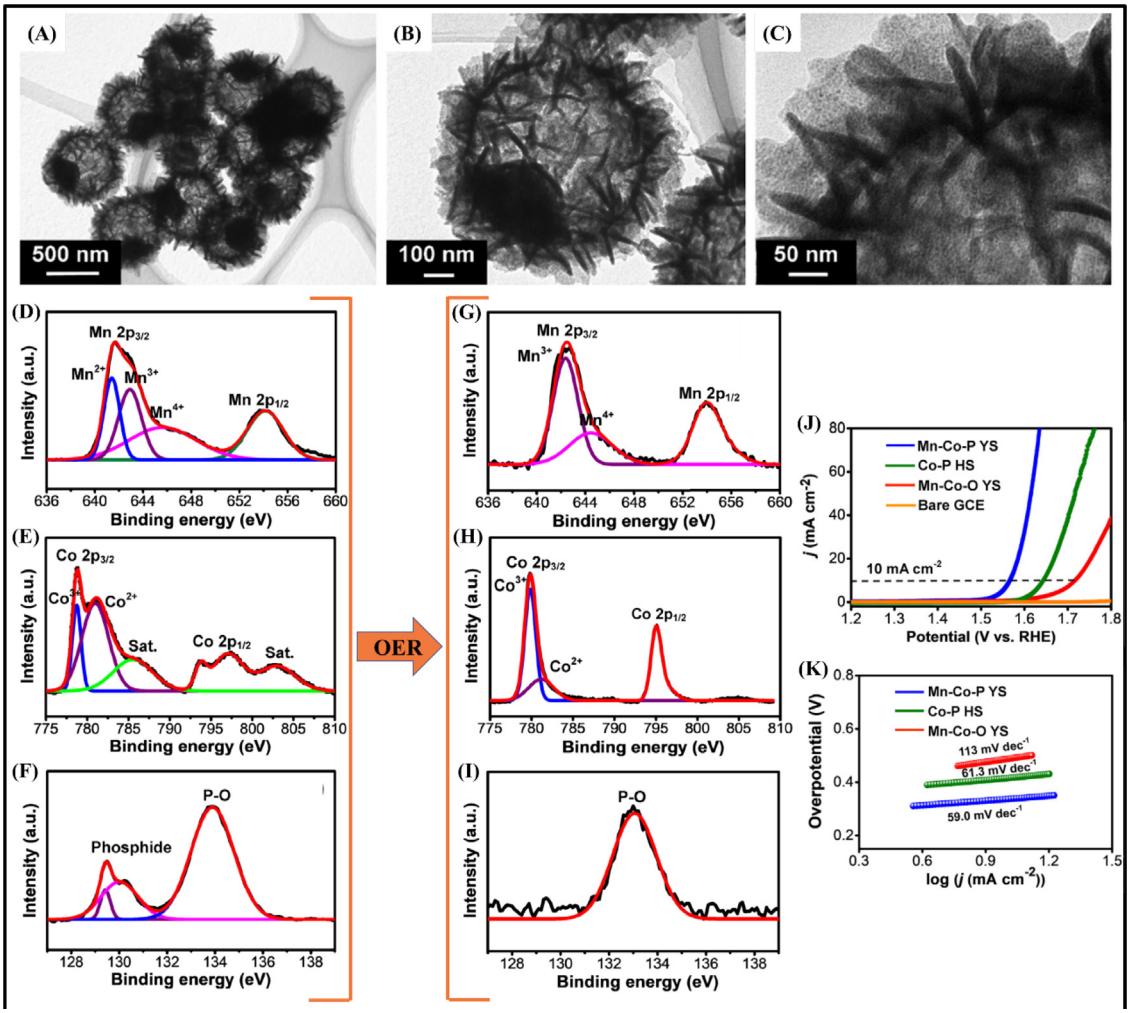


**Fig. 14.** (A) Low and, (B, C) high-magnification TEM images of Mn-Co-P YS. XPS spectra of Mn-Co phosphide yolk-shell catalyst before (D-F) and after OER (G-I) for (D, G) Mn 2p, (E, H) Co 2p, and (F, I) P 2p. (J) Polarization curves and (K) Tafel plots of the electrocatalytic material. Reproduced with permission from ref. [117]. Copyright © 2020 Elsevier B.V. All rights reserved.

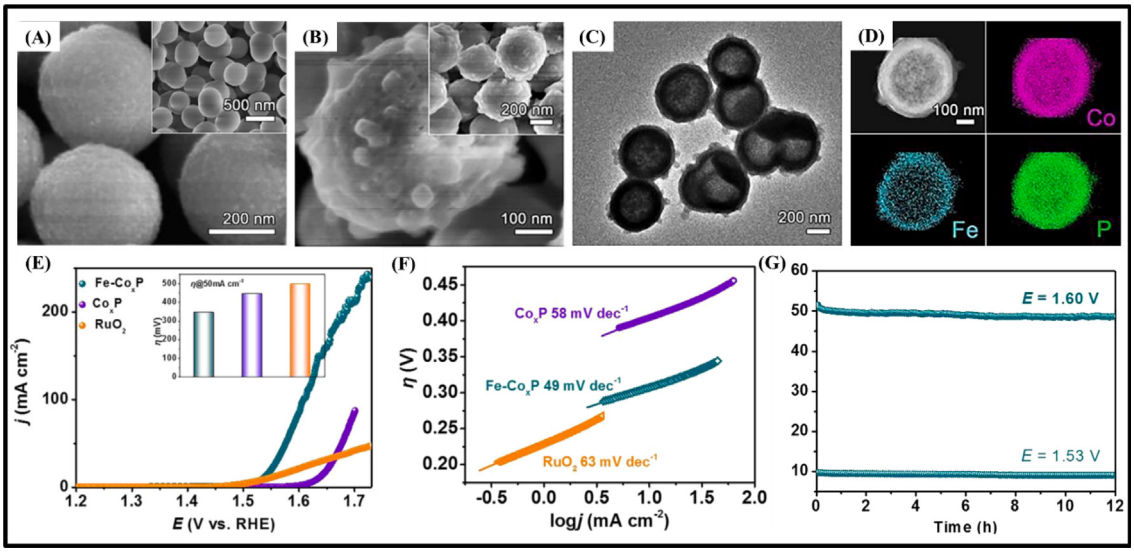


**Fig. 15.** SEM image of (A) Co-glycerolate and (B) Fe-$Co_xP$ after synthesis. (C) HRTEM image and (D) elemental mapping images of Fe-$Co_xP$ (E) Polarization curves and (F) Tafel plots of Fe-$Co_xP$ compared with $Co_xP$ and $RuO_2$. (G) Chronoamperometric curves of the electrocatalysts at a constant potential of 1.53 V and 1.60 V. Reproduced with permission from ref. [119]. Copyright © 2020 Elsevier B.V. All rights reserved.

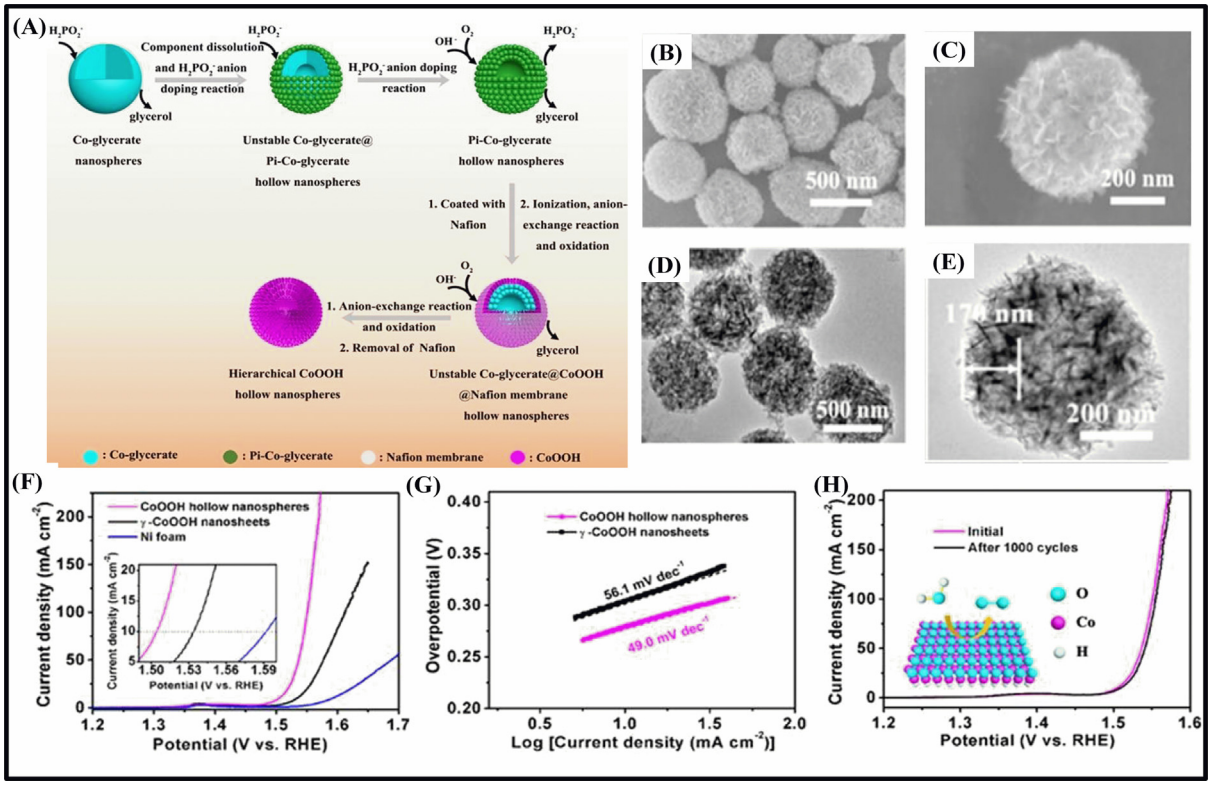


**Fig. 16.** (A) Schematic illustration of the synthesis of the hierarchical ultrathin sheet-based CoOOH hollow nanospheres. (B, C) SEM images and (D, E) TEM images of the material. (F) Polarization curves of the hierarchical CoOOH hollow nanospheres (magenta), γ-CoOOH nanosheets (black), and Ni foam (blue). (G) Tafel plots of the hierarchical CoOOH hollow nanospheres (magenta) and γ-CoOOH nanosheets (black). (H) Polarization curves of the hierarchical CoOOH hollow nanosphere catalyst recorded before (magenta) and after (black) 1000 sweeps. Inset shows the schematic illustration of electrocatalytic oxygen evolution process by the CoOOH hollow nanospheres. Reproduced with permission from ref. [120]. Copyright Marketplace™, Royal Society of Chemistry. (For interpretation of the references to colour in this figure legend, the reader is referred to the web version of this article.)

Hollow cobalt oxyhydroxide nanospheres rich in oxygen vacancies were prepared at room-temperature by self-template strategy (Fig. 16**A**). The ultrathin nanosheets and abundant oxygen vacancies provide high density of catalytic sites to the material (Fig. 16**B-16E**), shortened charge/ion diffusion path, reduced resistance to charge transport, good stability and extraordinary electrocatalytic activity for OER [120]. A CoOOH exhibiting good OER catalytic activity, with low overpotential of 275 mV and Tafel slope of only 49 mV dec$^{-1}$ (Fig. 16**F-16G**) was prepared by the authors. The material shows excellent activity even after 1000 cycles (Fig. 16**H**) and no change in potential, at the current density of 10 mA cm$^{-2}$ and 100 mA cm$^{-2}$, even after 12 h. They prepared a similar material, γ-CoOOH, previously reported in the literature [135], and compared it with the hierarchical ultrathin sheet-based CoOOH hollow nanospheres showing its superior properties (Fig. 16**F-16G**).

In addition to monometallic hydroxides/oxyhydroxide, layered double hydroxide (LDH) are also cited as excellent catalysts for OER, especially those containing two or more dissimilar metals [130,136]. LDHs exhibit a 2D layered nanosheet structure constituted by layers of octahedrally metal ions coordinated with edge-sharing hydroxyl groups perpendicular to the plane generating hydroxyl stacked interlayer space [137–139], where anions successfully intercalate. Using this class of material, Septiani *et al.* [124] reported the preparation of a holey assembly of 2D iron-doped nickel–cobalt LDH nanosheets (NiCo-Fe LDH) (Fig. 17**C-17F**) and its catalytic activity for OER. The catalyst was obtained by hydro/solvothermal reactions using NiCo-glycerolate spheres (Fig. 17**A-17B**) as self-templates. Regarding the activity for OER (Fig. 17**G-17I**), NiCo-Fe LDH exhibit an overpotential of 285 mV at a current density of 10 mA cm$^{-2}$ and Tafel slope of 62 mV dec$^{-1}$. The catalyst showed stability of 12 h under OER conditions. Such good results were attributed to enhanced ion transport and electrical conductivity promoted by iron doping and synergistic effects, and provision of many active sites for the OER conferred by the large specific surface area of the holey nanosheets. The presence of trivalent $Fe^{3+}$ ions can change the oxidation state of Co and Ni cation and induce metal vacancies as verified by XPS analysis [140]. In addition, the $Fe^{3+}$ cation doping is favored by the presence of $Ni^{2+}$ and $Co^{2+}$ ions [114]. However, the presence of metal ion species in different oxidation states are able to potentiate the electrical conductivity, enhancing the activity for OER [141]. The $Fe^{3+}$ ions can replace $Ni^{2+}$ ions and occupy the octahedral sites in the NiOOH structure changing the oxidation state of Ni or Co and induce the formation of metal vacancies, distort the octahedral coordination geometry, broaden the *d* bands, and improve the orbital overlapping. In short, the decrease in the coordination number of neighboring catalytic sites synergistically improves the adsorption of the OER intermediate (O*) and the electrocatalytic activity of NiCo-Fe LDH [124,140].

As reported earlier, M−glycerolates are normally used as precursors for preparation of many other classes of materials. However, its direct application as electrode materials has not been largely reported, especially for energy storage devices. On the other hand, the use of M−glycerolate, or other metal alkoxide-based materials, have received significant attention as electrocatalysts for OER because of the structural advantages perceived in materials based on stacked layers of metal – glycerolate, exhibiting well-organized organic and inorganic portions [12] suitable for the design of electroactive materials for different applications [18,19]. As already mentioned before, M−glycerolate based mate-

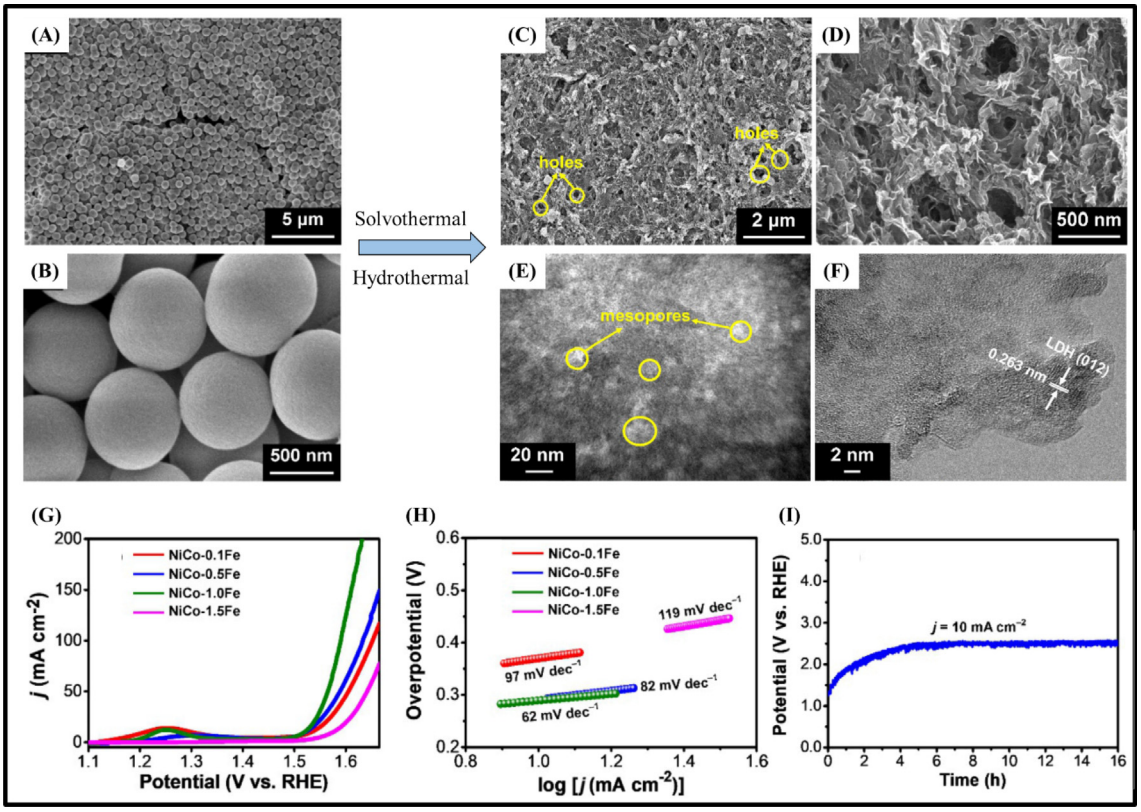


**Fig. 17.** (A and B) SEM images of NiCo-glycerolate and (C and D) NiCo-Fe LDH. TEM (E) and HRTEM (F) images of Fe-doped NiCo-Fe LDH nanosheets. (G) Polarization curves and (H) Tafel plots of NiCo-Fe LDH compared with different proportions of doping agents. (I) Long-term stability test of the electrocatalyst performed under a constant current density of 10 mA $cm^{-2}$. Reproduced with permission from ref. [124]. Copyright © 2019 Wiley-VCH Verlag GmbH & Co. KGaA, Weinheim.

rials tend to be converted to the corresponding metal oxyhydroxide based material exhibiting excellent electrocatalytic activity, under alkaline conditions.

The regular ordered microcomposition of the metal glycerolate-based materials, allied with controlled anion substitution reaction in mild conditions, mostly preserving the host structure thus acting as templates, allows the development of heterostructures, design of structural defects, formation of binary or multiple compounds and doping with other metal ions to improve the intrinsic activity of the electrocatalyst [12]. Based on that, Wang and co-workers [18] synthesized, *via* simple solvothermal process, layered bimetallic iron-nickel glycerolate microspheres (FeNiGly). The incorporation of Fe as a synergistic component, induced partial charge transfer and activation of the sites surrounded by Ni, increasing the density of charge carriers and improving the OER electrocatalytic activity. Accordingly, the resultant material showed an overpotential of 320 mV at a current density of 10 mA $cm^{-2}$ and Tafel slope of 50 mV $dec^{-1}$. The post-OER, XPS and XRD analyses confirmed the presence of Fe(Ni)OOH, both metal ions in the 3 + oxidation state. The metal glycerolates and metal (oxy)hydroxides electrocatalysts exhibit excellent hydrophilicity and have an interlayer space that easily accommodates and improves the adsorption of water and other OER reagents and intermediates on the surface. The incorporation of iron in the structure generates strong electronic interactions between Fe and Ni, optimizing the energetics of the OER activated complex and reducing the required overpotential for OER, thus boosting the electrocatalytic activity of the Fe(Ni)OOH phase [18,142,143].

In the same line, Dong and his collaborators [125] reported the synthesis of Cobalt Iron-glycerolate hollow spheres organized by nanosheets (CoFeG-HS) by an one-pot template-free solvothermal method (Fig. 18**A-18E**). The material exhibited an excellent electrochemical performance, with an overpotential of 242 mV at 10 mA $cm^{-2}$ and Tafel slope of 50 mV $dec^{-1}$ (Fig. 18**F-18H**). The hollow spheres have low density and high shell permeability providing fast diffusion and easy access to active sites, facilitating the OER process. The good catalytic activity of the material was also attributed to the formation of oxyhydroxide species on the surface, as confirmed by XPS analysis. The overall OER reaction mechanism in conventional catalysts consists of 5 steps (Fig. 18**I**), but the formation of M−OOH on the surface reduces the number of steps to two thus improving the reaction kinetics (Fig. 18**J**) [125]. In addition, the good catalytic activity can also be attributed to the synergistic effect between $Fe^{3+}$ and $Co^{2+}$, which is evidenced by comparing the performances of CoFeG-HS, Co-glycerolate and Fe-glycerolate (Fig. 18**F-18H**). In fact, the catalytic activity reported for the CoFeG-HS is superior to the CoCuFe-Gly hollow sphere prepared by Moradi *et al.* [11] which exhibited an overpotential of 317 mV at 10 mA mA $cm^{-2}$ and a Tafel slope of 69 mV $dec^{-1}$.

At this point, it is evident the tendency towards multimetallic systems to take advantage of the synergic effects between the components [144] to enhance the electrocatalytic performance of materials for water oxidation. For instance, Nguyen and co-workers [122] prepared high entropy materials (HEM) *via* a simple solvothermal process starting with a high entropy glycerolate (HEG) with 5 different metals, FeNiCoCrMn-G (Fig. 19**A**). Thanks to the layered structure similar to anion intercalated hydroxides and generous interlayer spacing, the reagents are easily accommodated thus facilitating the OER process. The electrochemical measurements (Fig. 19**B-19G**) indicated an overpotential of 229 mV at a current density of 10 mA $cm^{-2}$ and a Tafel slope of 40 mV $dec^{-1}$, that showed no significant changes after 36 h of test. The evaluation of similar systems with different metallic compositions,

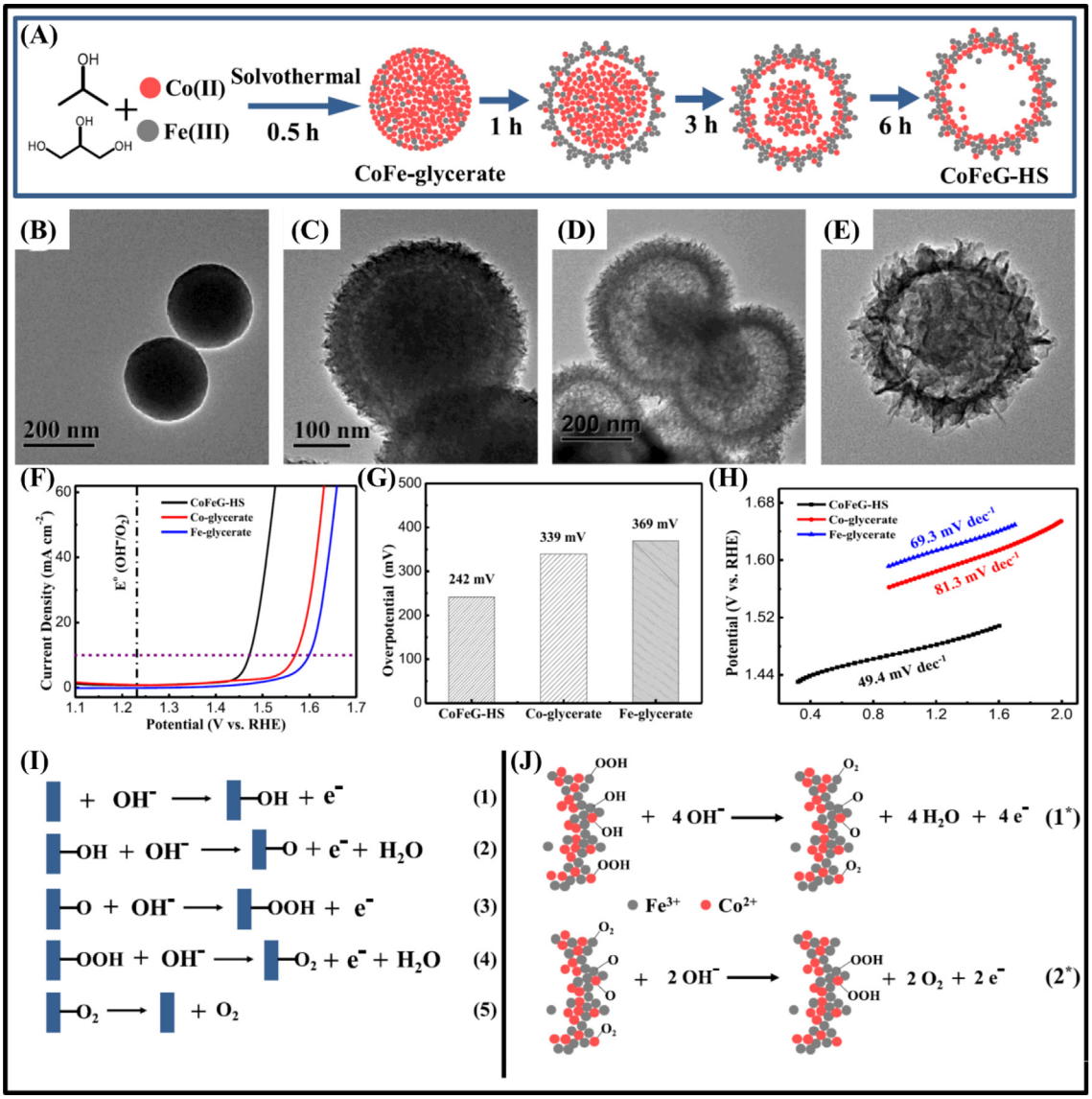


**Fig. 18.** (A) Scheme showing the evolution of the CoFeG-Hs electrocatalyst synthesis as a function of the reaction time and (B-E) the respective TEM images of the corresponding intermediate products taken after 0.5, 1, 3, and 6 h of reaction. (F) Polarization curves of CoFeG-HS, Co-glycerolate, and Fe-glycerolate in 1.0 M KOH at a scan rate of 50 mV $s^{-1}$. (G) Comparison of the overpotentials of the samples and (H) corresponding Tafel slopes. Scheme showing the mechanism of the electrochemical OER: (I) the elementary reactions of the general mechanism, where the blue squares represent the surface of the catalyst, while the active metal sites was represented as 'M' in the manuscript; (J) (1*−2*) are the elementary steps for CoFeG-HS with M−OOH sites on the surface. Reproduced with permission from ref. [125]. Copyright © 2020 American Chemical Society. (For interpretation of the references to colour in this figure legend, the reader is referred to the web version of this article.)

as can be seen in the Fig. 19**B-19G**, evidenced the perfect synergy of the metal sites of the HEG for OER electrocatalysis. The evaluation of density of states (Fig. 19**H**) showed that the FeNiCoCrMn-G electrocatalyst has more electronic states near and below the Fermi level than similar multi-metallic glycerolates, providing more hole states to promote the oxidation reaction. Interestingly, (Fig. 19**I**) HEG was demonstrated to be an amorphous material by XRD analysis, thus being able to provide more active sites for electrocatalysis and accelerate the charge transfer between active sites and the reaction intermediates. In fact, amorphous phases have a higher proportion of randomly oriented bonds with unsaturated electronic configurations which facilitates the adsorption and activation of the reagents [122,145]. It is important to mention that FeNiCoCrMn-G showed higher electrocatalytic activity than septenary HEG containing Cr, Mn, Fe, Co, Ni, Ti, and Zn (designated as 5MTZ) prepared by Ting and collaborators [118] (overpotential of 251 mV at 50 mA $cm^{-2}$ and a Tafel slope of 42.3 mV $dec^{-1}$). In short, this work evidenced the relevance of amorphous phase and synergistic effects between the transition metal ions to realize high performance electrocatalysts that can serve as alternatives for the noble metal-based materials.

## 7. Summary and outlook

M−glycerolates are auspicious precursors for the design and preparation of a large variety of electrode materials for energy technology applications owing to their distinct structures and morphologies, chemical composition, as well as electrical and electrochemical properties. The M−glycerolates are not extensively explored but the materials prepared from them are promising candidates as electrode materials of supercapacitors and batteries, as well as electrocatalysts for water-splitting, as discussed in this review article.

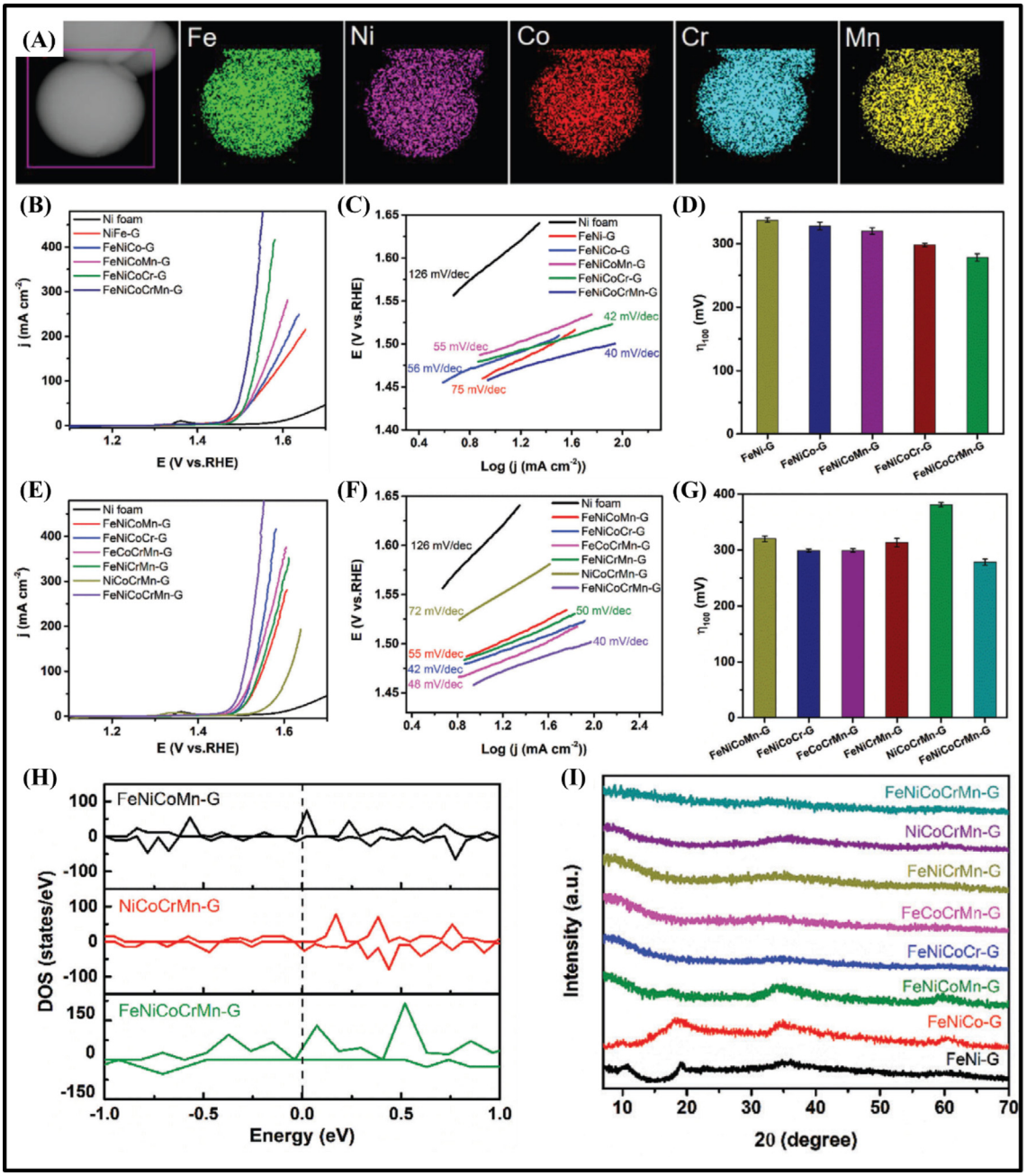


**Fig. 19.** (A) STEM-EDS mappings of FeNiCoCrMn-G. (B-D) LSV Curves, Tafel plots and overpotentials, respectively, of the first group of metal glycerolates. (E-G) LSV Curves, Tafel plots and overpotentials, respectively, of the second group of metal glycerolates. (H) Calculated density of states and (I) XRD profiles of multi-metal glycerolates. Reproduced with permission from ref. [122]. Copyright © 2021 The Authors. Advanced Science published by Wiley-VCH GmbH.

Several well-established synthesis methods are available to prepare micro- and nanostructured M−glycerolates and derived metal hydroxides, metal oxides, metal sulfides, metal phosphides, and metal selenides among other materials, prepared as hollow spheres, yolk shelled hollow spheres, ball-in-ball hollow spheres and 2D morphology materials were discussed.

The materials with spherical layered structures derived from M−glycerolates show high capacitance, rate capability and cycling retention for application in supercapacitor devices. Such enhanced properties are generally ascribed to the efficient accommodation of volume expansion, the reduced diffusion path of electrolyte ions, and presence of structural voids as ion reservoirs. In addition, composite materials constituted by M−glycerolate derived materials and carbonaceous materials such as graphene, reduced graphene oxide among others, showing very strong synergic effects can be easily prepared in few steps. In this context, trimetallic materials derived from M−glycerolates showed the highest energy and power densities (62.54 Wh $kg^{-1}$ and 42.307 kW $kg^{-1}$) in supercapacitors devices, highlighting the importance of the synergic effect of Mn, V and Cu on common Ni and Co based materials, where copper precursors are showing obvious advantages.

M−glycerolates derived materials also exhibit wide application in metal ion batteries such as LIBs and SIBs. In fact, many Ni, Co and Mo mono- and bimetallic glycerolates were used in the preparation of several M−glycerolates derived materials, such as metal sulfides, metal phosphides, metal selenides and especially metal oxides. However, the main trend and promising application is in the development of carbon-coated M−glycerolates derived materi-

als that have emerged as very high conductivity electrode materials while acting as adhesives to improve the structural integrity during charging/discharging processes.

The regularly ordered microcomposition of the metal glycerolate-based materials, allied with the possibility of anion substitution reaction in a controlled way, while preserving the structure thus acting as templates, allows the development of heterostructures, design of material with engineered structural defects, as well as preparation of multi-metallic materials to improve the intrinsic activity of the electrocatalyst by electronic activation and synergic effects. In fact, the incorporation of elements such as iron in the structure can induce strong electronic interactions with other metal ions next to it, changing their oxidation state and creating coordination vacancies, decreasing the energy of the activated complex and the overpotential for OER. The overall OER reaction mechanism conventionally taking place in 5 steps (Fig. 18**I)** can be simplified to two steps by the adsorption of M−OOH on the surface, thus boosting the electrocatalytic activity. Furthermore, the higher density of randomly oriented unsaturated bonds in amorphous materials can be exploited in parallel with the excellent hydrophilicity and interlayer spacing of metal glycerolates and metal (oxy)hydroxides to facilitate the adsorption and activation of reagents.

Despite the significant research efforts in recent years to prepare M−glycerolates derived electrode materials by exploiting their composition and structural tunability, there are still some challenges and bottlenecks that need to be sorted out to realize the mass production, practical application and commercialization of the next generation of energy technologies. In fact, to overcome the significant limitations and challenges some future perspectives and directions are discussed as follows and summarized in the Scheme 2:

1. Despite several reports on the syntheses and characterization of M−glycerolates and their derived materials, the mechanism of formation of their lamellar structure has not been investigated in much detail. In fact, a fundamental experimental and theoretical understanding on the coordination chemistry of glycerol and metal ions is still necessary. In addition, advanced *in-situ* and *in-operando* characterization techniques are key to obtaining real-time information about the intermediates and reaction mechanism [146], as well as degradation mechanisms of the electrode materials. Among them, advanced spectroscopic techniques employing synchrotron light such as Extended X-ray Absorption Fine Structure (EXAFS), X-ray Absorption Near-Edge Structure (XANES) and Near Edge X-ray Absorption Fine Structure (NEXAFS), XPS, Resonant Inelastic X-ray Scattering (RIXS), among others are of great importance to unravel the true structure of M−glycerolate derived materials.
2. Generally, M−glycerolates and their derived materials are characterized as spheres with a size outside the nanometer scale. Thus, new preparation methods to get M−glycerolate based materials with less than 100 nm are highly desired, since their properties should be differentiated and highly promising, not only due to the larger surface area but especially for the emergence of unique nanometer scale properties.
3. The development of tri- and multi-metallic, and/or high-entropy electrode materials is a trend in the field of energy application. However, there is still much research to be done in the development of such a system based on M−glycerolates derived electrode materials.
4. The design of new composite materials is highly desired. Furthermore, the optimization of the mass ratio of electroactive materials/conductive materials is crucial for obtaining materials with higher energy and power densities [9].
5. The development of metal oxides or metal oxide-based composites derived from M−glycerolates usually goes through an annealing process at high temperatures, which is an expensive and time-consuming step, especially considering the large-scale production of affordable electrode materials for energy storage or conversion. In this context, the use of reagentless laser-based techniques in the synthesis [147] and improvement of electrode materials [148] is an excellent alternative since it is a simple and fast synthetic process [3,9].

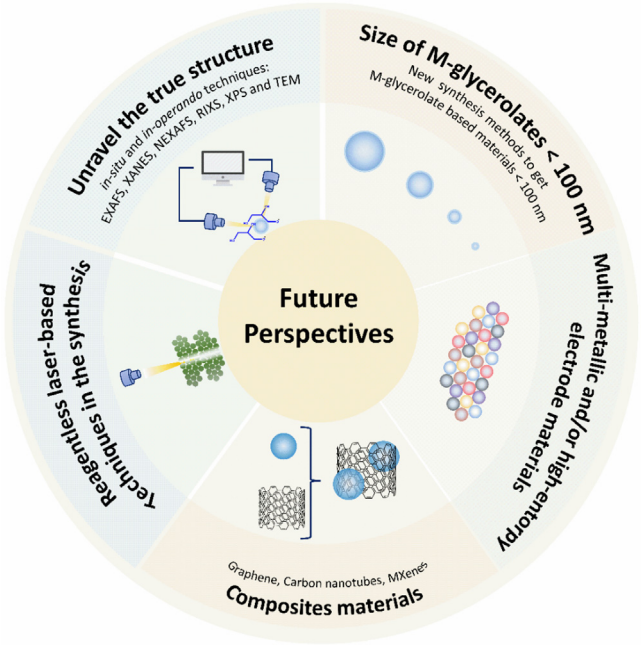


**Scheme 2.** Schematic illustration showing a few possible research directions and great opportunities that deserve continuous attention for the next generation of electrode materials based on M−glycerinates.

In short, the recent progress in the use of metal-glycerolate electrode materials in energy technologies reveals promising advances, yet still there is much to be done to catch the needs of our energy hungry society.

## Data availability

Data will be made available on request.

## Declaration of Competing Interest

The authors declare that they have no known competing financial interests or personal relationships that could have appeared to influence the work reported in this paper.

## Acknowledgments

This work was supported by the Sao Paulo Research Foundation (FAPESP 2018/21489-1, 2017/13137-5, and 2013/24725-4) and the National Council for Scientific and Technological Development (CNPq 311847-2018-8, 303137/2016-9, 401581/2016-0, 408222/2016-6, and 442599/2019-6), in addition to the fellowships granted to J.M.G. (FAPESP 2018/16896-7 and 2020/06176-7). R. Shahbazian-Yassar acknowledges the financial support from National Science Foundation (NSF) award number DMR-1809439.

## References


[1] X. Guo, C. Chen, Y. Zhang, Y. Xu, H. Pang, The application of transition metal cobaltites in electrochemistry, Energy Stor. Mater. 23 (2019) 439–465, https://www.sciencedirect.com/science/article/pii/S2405829719302983.

[2] X.-Y. Liu, K.-X. Wang, J.-S. Chen, Template-directed metal oxides for electrochemical energy storage, Energy Stor. Mater. 3 (2016) 1–17, https://www.sciencedirect.com/science/article/pii/S2405829715300921.

[3] J.G. Ruiz-Montoya, V.L. Quispe-Garrido, J.C. Calderón Gómez, A.M. Baena Moncada, J.M. Gonçalves, Recent Progress and Prospects on Supercapacitor Materials based on Metal Oxide or Hydroxide/Biomass-Derived Carbon Composites, Sustain. Energy Fuels, 5 (2021) 5332 - 5365. http://dx.doi.org/10.1039/D1SE01170G.

[4] J.M. Gonçalves, M.N.T. Silva, K.K. Naik, P.R. Martins, D.P. Rocha, E. Nossol, R.A. A. Munoz, L. Angnes, C.S. Rout, Multifunctional spinel $MnCo_2O_4$ based materials for energy storage and conversion: a review on emerging trends, recent developments and future perspectives, J. Mater. Chem. A 9 (2021) 3095–3124, https://doi.org/10.1039/D0TA11129E.

[5] J.M. Gonçalves, P.R. Martins, K. Araki, L. Angnes, Recent progress in water splitting and hybrid supercapacitors based on nickel-vanadium layered double hydroxides, J. Energy. Chem., 57 (2021) 496-515. https://www.sciencedirect.com/science/article/pii/S2095495620306100.

[6] J.M. Gonçalves, P.R. Martins, D.P. Rocha, T.A. Matias, M.S.S. Julião, R.A.A. Munoz, L. Angnes, Recent trends and perspectives in electrochemical sensors based on MOF-derived materials, J. Mater. Chem. C 9 (2021) 8718–8745, https://doi.org/10.1039/D1TC02025K.

[7] J.M. Gonçalves, P.R. Martins, B.G. Santos, K. Araki, L. Angnes, Sensing Materials: Metals Oxides, Reference Module in Biomedical Sciences 2 (2023) 98–113, https://doi.org/10.1016/B978-0-12-822548-6.00002-9, http://www.sciencedirect.com/science/article/pii/B9780128225486000029.

[8] R.R. Salunkhe, Y.V. Kaneti, Y. Yamauchi, Metal-Organic Framework-Derived Nanoporous Metal Oxides toward Supercapacitor Applications: Progress and Prospects, ACS Nano 11 (2017) 5293–5308, https://doi.org/10.1021/acsnano.7b02796.

[9] M.I. da Silva, Í.R. Machado, H.E. Toma, K. Araki, L. Angnes, J.M. Gonçalves, Recent progress in water-splitting and supercapacitor electrode materials based on MOF-derived sulfides, J. Mater. Chem. A 10 (2022) 430–474, https://doi.org/10.1039/D1TA05927K.

[10] J.V. Braun, A.K. Alves, The Role of Glycerol in the Synthesis of Nanomaterials, in: A. Kopp Alves (Ed.), Technological Applications of Nanomaterials, Springer International Publishing, Cham, 2022, pp. 217–228, https://doi.org/10.1007/978-3-030-86901-4_14.

[11] M. Moradi, F. Hasanvandian, M. Ghahraman Afshar, A. Larimi, F. Khorasheh, E. Niknam, S. Rahman Setayesh, Incorporation of Fe in mixed CoCu-alkoxide hollow sphere for enhancing the electrochemical water oxidation performance, Mater. Today Chem. 22 (2021). https://www.sciencedirect.com/science/article/pii/S246851942100166X.

[12] X. Liu, M. Gong, S. Deng, T. Zhao, J. Zhang, D. Wang, Recent advances on metal alkoxide-based electrocatalysts for water splitting, J. Mater. Chem. A 8 (2020) 10130–10149, https://doi.org/10.1039/D0TA03044A.

[13] P.G. Slade, E.W. Radoslovich, M. Raupach, Crystal and molecular structure of cobalt (II) monoglycerolate, Acta. Crystallogr. B. Struct. Sci. Cryst. Eng. Mater. 27 (1971) 2432–2436, https://doi.org/10.1107/S0567740871005995.

[14] T.W. Hambley, M.R. Snow, The crystal and molecular structure of zinc(II) monoglycerolate, Aust. J. Chem. 36 (1983) 1249–1253, https://doi.org/10.1071/CH9831249.

[15] H.L. Keller, H.J. Riebe, Darstellung und Kristallstruktur von Blei(II)-monoglycerat, Z. Anorg. Allg. Chem. 550 (1987) 102–108, https://doi.org/10.1002/zaac.19875500711.

[16] J. Teichert, T. Block, R. Pöttgen, T. Doert, M. Ruck, Tin and Lead Alkoxides of Ethylene Glycol and Glycerol and their Decomposition to Oxide Materials, Eur. J. Inorg. Chem. 2019 (2019) 3820–3831, https://doi.org/10.1002/ejic.201900755.

[17] T.y.G. Khonina, E.Y. Nikitina, A.Y. Germov, B.Y. Goloborodsky, K.N. Mikhalev, E.A. Bogdanova, D.S. Tishin, A.M. Demin, V.P. Krasnov, O.N. Chupakhin, V.N. Charushin, Individual iron(iii) glycerolate: synthesis and characterisation, Rsc Adv, 12 (2022) 4042-4046. http://dx.doi.org/10.1039/D1RA08485B.

[18] M. Wang, J. Jiang, L. Ai, Layered Bimetallic Iron-Nickel Alkoxide Microspheres as High-Performance Electrocatalysts for Oxygen Evolution Reaction in Alkaline Media, ACS Sustain. Chem. Eng. 6 (2018) 6117–6125, https://doi.org/10.1021/acssuschemeng.7b04784.

[19] D. Larcher, G. Sudant, R. Patrice, J.M. Tarascon, Some Insights on the Use of Polyols-Based Metal Alkoxides Powders as Precursors for Tailored Metal-Oxides Particles, Chem. Mater. 15 (2003) 3543–3551, https://doi.org/10.1021/cm030048m.

[20] Y. Zheng, H. Geng, Y. Zhang, L. Chen, C.C. Li, Precursor-Based Synthesis of Porous Colloidal Particles towards Highly Efficient Catalysts, Chem Eur J 24 (2018) 10280–10290, https://doi.org/10.1002/chem.201800625.

[21] N. Mir, M. Salavati-Niasari, F. Davar, Preparation of ZnO nanoflowers and Zn glycerolate nanoplates using inorganic precursors via a convenient rout and application in dye sensitized solar cells, Chem. Eng. J. 181–182 (2012) 779–789, https://www.sciencedirect.com/science/article/pii/S1385894711014872.

[22] R. Rémiás, Á. Kukovecz, M. Darányi, G. Kozma, S. Varga, Z. Kónya, I. Kiricsi, Synthesis of Zinc Glycerolate Microstacks from a ZnO Nanorod Sacrificial Template, Eur. J. Inorg. Chem. 2009 (2009) 3622–3627, https://doi.org/10.1002/ejic.200900308.

[23] Y.F. Yuan, W.C. Zhao, L. Chen, G.S. Cai, S.Y. Guo, CoO hierarchical mesoporous nanospheres@$TiO_2$@C for high-performance lithium-ion storage, Appl. Surf. Sci. 556 (2021), https://www.sciencedirect.com/science/article/pii/S0169433221008862.

[24] C. Cheng, C. Wei, Y. He, L. Liu, J. Hu, W. Du, Etching strategy synthesis of hierarchical Ni-Mn hydroxide hollow spheres for supercapacitors, J. Energy Stor. 33 (2021), https://www.sciencedirect.com/science/article/pii/S2352152X20319356.

[25] M. Amiri, S.S.H. Davarani, S.K. Kaverlavani, S.E. Moosavifard, M. Shamsipur, Construction of hierarchical nanoporous $CuCo_2V_2O_8$ hollow spheres as a novel electrode material for high-performance asymmetric supercapacitors, Appl Surf Sci 527 (2020) 146855. https://www.sciencedirect.com/science/article/pii/S0169433220316123.

[26] Z. Liu, F. Teng, C. Yuan, Z. Ul Abideen, W. Gu, Z. Liu, Highly Uniform MnCo2O4 Hollow Spheres-Based All-Solid-State Asymmetric Micro-Supercapacitor via a Simple Metal-Glycerate Precursor Approach, Energy Technol-Ger, 7 (2019) 1900314. https://doi.org/10.1002/ente.201900314.

[27] L. Shen, L. Yu, X.-Y. Yu, X. Zhang, X.W. Lou, Self-Templated Formation of Uniform $NiCo_2O_4$ Hollow Spheres with Complex Interior Structures for Lithium-Ion Batteries and Supercapacitors, Angew. Chem. Int. Ed. 54 (2015) 1868–1872, https://doi.org/10.1002/anie.201409776.

[28] C. Wei, Q. Chen, C. Cheng, R. Liu, Q. Zhang, L. Zhang, Mesoporous nickel cobalt manganese sulfide yolk–shell hollow spheres for high-performance electrochemical energy storage, Inorg. Chem. Front. 6 (2019) 1851–1860, https://doi.org/10.1039/C9QI00173E.

[29] L. Shen, L. Yu, H.B. Wu, X.-Y. Yu, X. Zhang, X.W. Lou, Formation of nickel cobalt sulfide ball-in-ball hollow spheres with enhanced electrochemical pseudocapacitive properties, Nat. Commun. 6 (2015) 6694, https://doi.org/10.1038/ncomms7694.

[30] Y.H. Lee, B.K. Kang, M.S. Kim, H.W. Choi, D.S. Choi, M. Kumar, D.H. Yoon, Synthesis and Characterization of Highly Uniform $CuCo_2S_4$ Ball-in-Ball Hollow Nanospheres as High Performance Electrode for Supercapacitors, Phys. Status Solidi A 215 (2018) 1700936, https://doi.org/10.1002/pssa.201700936.

[31] Y. Zhao, Z. Shi, H. Li, C.-A. Wang, Designing pinecone-like and hierarchical manganese cobalt sulfides for advanced supercapacitor electrodes, J. Mater. Chem. A 6 (2018) 12782–12793, https://doi.org/10.1039/C8TA02438C.

[32] N.L. Wulan Septiani, Y.V. Kaneti, K.B. Fathoni, J. Wang, Y. Ide, B. Yuliarto, H.K. Nugraha, A.K. Dipojono, D. Nanjundan, Y. Golberg, Y.Y. Bando, Self-assembly of nickel phosphate-based nanotubes into two-dimensional crumpled sheet-like architectures for high-performance asymmetric supercapacitors, Nano Energy 67 (2020), https://www.sciencedirect.com/science/article/pii/S2211285519309772.

[33] T. Dong, X. Zhang, P. Wang, H.-S. Chen, P. Yang, Hierarchical nickel-cobalt phosphide hollow spheres embedded in P-doped reduced graphene oxide towards superior electrochemistry activity, Carbon 149 (2019) 222–233, https://www.sciencedirect.com/science/article/pii/S0008622319303847.

[34] X. Zhang, Y. Xiong, M. Dong, Z. Hou, Y. Qian, Construction of hierarchical $MoSe_2$@C hollow nanospheres for efficient lithium/sodium ion storage, Inorg. Chem. Front. 7 (2020) 1691–1698, https://doi.org/10.1039/D0QI00017E.

[35] Y.V. Kaneti, R.R. Salunkhe, N.L. Wulan Septiani, C. Young, X. Jiang, Y.-B. He, Y.-M. Kang, Y. Sugahara, Y. Yamauchi, General template-free strategy for fabricating mesoporous two-dimensional mixed oxide nanosheets via self-deconstruction/reconstruction of monodispersed metal glycerate nanospheres, J. Mater. Chem. A 6 (2018) 5971–5983, https://doi.org/10.1039/C8TA00008E.

[36] Y. Zhao, Z. Shi, T. Lin, L. Suo, C. Wang, J. Luo, Z. Ruan, C.-A. Wang, J. Li, Brownian-snowball-mechanism-induced hierarchical cobalt sulfide for supercapacitors, J. Power Sources 412 (2019) 321–330, https://www.sciencedirect.com/science/article/pii/S0378775318313028.

[37] T. Cui, S. Wu, S. Zhou, Q. Feng, X. Xu, H. Zhao, Q. Su, Y. Wang, X. Zhao, Q. Yang, Three-dimensional microsphere-like cobalt-glycerolate strutted nickel hydroxidenitrate nanoflakes grown by hydrothermal method for asymmetric hybrid supercapacitors, J. Energy Stor. 52 (2022), https://www.sciencedirect.com/science/article/pii/S2352152X22007411.

[38] Y. Wang, Y. Song, Y. Xia, Electrochemical capacitors: mechanism, materials, systems, characterization and applications, Chem. Soc. Rev. 45 (2016) 5925–5950, https://doi.org/10.1039/C5CS00580A.

[39] J. Sun, C. Wu, X. Sun, H. Hu, C. Zhi, L. Hou, C. Yuan, Recent progresses in high-energy-density all pseudocapacitive-electrode-materials-based asymmetric supercapacitors, J. Mater. Chem. A 5 (2017) 9443–9464, https://doi.org/10.1039/C7TA00932A.

[40] M. Huang, F. Li, F. Dong, Y.X. Zhang, L.L. Zhang, $MnO_2$-based nanostructures for high-performance supercapacitors, J. Mater. Chem. A 3 (2015) 21380–21423, https://doi.org/10.1039/C5TA05523G.

[41] M. Okubo, A. Sugahara, S. Kajiyama, A. Yamada, MXene as a Charge Storage Host, Acc. Chem. Res. 51 (2018) 591–599, https://doi.org/10.1021/acs.accounts.7b00481.

[42] I. Shown, A. Ganguly, L.-C. Chen, K.-H. Chen, Conducting polymer-based flexible supercapacitor, Energy Sci. Eng. 3 (2015) 2–26, https://doi.org/10.1002/ese3.50.

[43] T. Brousse, D. Bélanger, J.W. Long, To Be or Not To Be Pseudocapacitive?, J Electrochem Soc, 162 (2015) A5185-A5189. http://jes.ecsdl.org/content/162/5/A5185.abstract.

[44] H. Xia, Y. Shirley Meng, G. Yuan, C. Cui, L. Lu, A Symmetric $RuO_2/RuO_2$ Supercapacitor Operating at 1.6 V by Using a Neutral Aqueous Electrolyte, Electrochem. Solid St. 15 (2012) A60, https://doi.org/10.1149/2.023204esl.

[45] J.J. Yoo, K. Balakrishnan, J. Huang, V. Meunier, B.G. Sumpter, A. Srivastava, M. Conway, A.L. Mohana Reddy, J. Yu, R. Vajtai, P.M. Ajayan, U.P.G. Supercapacitors, Nano Lett. 11 (2011) 1423–1427, https://doi.org/10.1021/nl200225j.

[46] F. Wang, S. Xiao, Y. Hou, C. Hu, L. Liu, Y. Wu, Electrode materials for aqueous asymmetric supercapacitors, RSC Adv. 3 (2013) 13059–13084, https://doi.org/10.1039/C3RA23466E.

[47] A.-L. Brisse, P. Stevens, G. Toussaint, O. Crosnier, T. Brousse, $Ni(OH)_2$ and NiO Based Composites: Battery Type Electrode Materials for Hybrid Supercapacitor Devices, Materials 11 (2018) 1178, https://www.mdpi.com/1996-1944/11/7/1178.

[48] A. Kanwade, S. Gupta, A. Kankane, M.K. Tiwari, A. Srivastava, J.A. Kumar Satrughna, S. Chand Yadav, P.M. Shirage, Transition metal oxides as a cathode for indispensable Na-ion batteries, RSC Adv. 12 (2022) 23284–23310, https://doi.org/10.1039/D2RA03601K.

[49] V. Augustyn, P. Simon, B. Dunn, Pseudocapacitive oxide materials for high-rate electrochemical energy storage, Energ, Environ. Sci. 7 (2014) 1597–1614, https://doi.org/10.1039/C3EE44164D.

[50] A. Chakraborty, S. Kunnikuruvan, S. Kumar, B. Markovsky, D. Aurbach, M. Dixit, D.T. Major, Layered Cathode Materials for Lithium-Ion Batteries: Review of Computational Studies on $LiNi_{1-x-y}Co_xMn_yO_2$ and $LiNi_{1-x-y}Co_xAl_yO_2$, Chem. Mater. 32 (2020) 915–952, https://doi.org/10.1021/acs.chemmater.9b04066.

[51] D.P. Chatterjee, A.K. Nandi, A review on the recent advances in hybrid supercapacitors, J. Mater. Chem. A 9 (2021) 15880–15918, https://doi.org/10.1039/D1TA02505H.

[52] D.P. Dubal, O. Ayyad, V. Ruiz, P. Gómez-Romero, Hybrid energy storage: the merging of battery and supercapacitor chemistries, Chem. Soc. Rev. 44 (2015) 1777–1790, https://doi.org/10.1039/C4CS00266K.

[53] J.B. Goodenough, How we made the Li-ion rechargeable battery, Nat. Electron., 1 (2018) 204-204. https://doi.org/10.1038/s41928-018-0048-6.

[54] D. Qian, C. Ma, K.L. More, Y.S. Meng, M. Chi, Advanced analytical electron microscopy for lithium-ion batteries, NPG Asia Mater., 7 (2015) e193-e193. https://doi.org/10.1038/am.2015.50.

[55] C. Zou, L. Zhang, X. Hu, Z. Wang, T. Wik, M. Pecht, A review of fractional-order techniques applied to lithium-ion batteries, lead-acid batteries, and supercapacitors, J. Power Sources 390 (2018) 286–296, https://www.sciencedirect.com/science/article/pii/S0378775318303768.

[56] P. Wang, B. Zhao, J. Bai, P. Tong, X. Zhu, Y. Sun, Transition Metal Nitrides in Lithium- and Sodium-Ion Batteries: Recent Progress and Perspectives, Adv. Mater. Interfaces, 9 (2022) 2200606. https://doi.org/10.1002/admi.202200606.

[57] D. Deb, G. Sai Gautam, Critical overview of polyanionic frameworks as positive electrodes for Na-ion batteries, J. Mater. Res. (2022), https://doi.org/10.1557/s43578-022-00646-7.

[58] D. Alvira, D. Antorán, J.J. Manyà, Plant-derived hard carbon as anode for sodium-ion batteries: A comprehensive review to guide interdisciplinary research, Chem. Eng. J. 447 (2022), https://www.sciencedirect.com/science/article/pii/S1385894722029564.

[59] A.P. Gomes, J.M. Gonçalves, K. Araki, P.R. Martins, Enhancement of Stability and Specific Charge Capacity of Alpha-$Ni(OH)_2$ by Mn(II) Isomorphic Substitution, Energy Technol-Ger 7 (2019) 1800980, https://doi.org/10.1002/ente.201800980.

[60] P.P. Lavela Cabello, Electrochimica Acta Editorial Recent Advances in Sodium Ion Batteries, Electrochim. Acta 431 (2022), https://doi.org/10.1016/j.electacta.2022.141140, https://www.sciencedirect.com/science/article/pii/S001346862201297X.

[61] H. Cheng, J.G. Shapter, Y. Li, G. Gao, Recent progress of advanced anode materials of lithium-ion batteries, J Energy Chem 57 (2021) 451–468, https://www.sciencedirect.com/science/article/pii/S2095495620306197.

[62] Y. Han, Y. Lei, J. Ni, Y. Zhang, Z. Geng, P. Ming, C. Zhang, X. Tian, J.-L. Shi, Y.-G. Guo, Q. Xiao, Single-Crystalline Cathodes for Advanced Li-Ion Batteries: Progress and Challenges, Small n/a (2022) 2107048, https://doi.org/10.1002/smll.202107048.

[63] Y. Lu, Q. Zhang, J. Chen, Recent progress on lithium-ion batteries with high electrochemical performance, Sci. China Chem. 62 (2019) 533–548, https://doi.org/10.1007/s11426-018-9410-0.

[64] J.M. Tarascon, M. Armand, Issues and challenges facing rechargeable lithium batteries, Nature 414 (2001) 359–367, https://doi.org/10.1038/35104644.

[65] J. Xu, Critical Review on cathode–electrolyte Interphase Toward High-Voltage Cathodes for Li-Ion Batteries, Nano-Micro Lett 14 (2022) 166, https://doi.org/10.1007/s40820-022-00917-2.

[66] Q. Wu, T. Zhang, J. Geng, S. Gao, H. Ma, F. Li, Anionic Redox Chemistry for Sodium-Ion Batteries: Mechanisms, Advances, and Challenges, Energy Fuel 36 (2022) 8081–8095, https://doi.org/10.1021/acs.energyfuels.2c01601.

[67] J.W. Ager, A.A. Lapkin, Chemical storage of renewable energy, Science 360 (2018) 707–708, https://www.science.org/doi/abs/10.1126/science.aat7918.

[68] V.R. Stamenkovic, D. Strmcnik, P.P. Lopes, N.M. Markovic, Energy and fuels from electrochemical interfaces, Nat. Mater. 16 (2017) 57–69, https://doi.org/10.1038/nmat4738.

[69] K.T. Møller, T.R. Jensen, E. Akiba, H.-W. Li, Hydrogen - A sustainable energy carrier, Prog. Nat. Sci.: Mater. Int. 27 (2017) 34–40, https://www.sciencedirect.com/science/article/pii/S1002007116303240.

[70] S. Masoudi Soltani, A. Lahiri, H. Bahzad, P. Clough, M. Gorbounov, Y. Yan, Sorption-enhanced Steam Methane Reforming for Combined $CO_2$ Capture and Hydrogen Production: A State-of-the-Art Review, Carbon Capture, Sci. Technol. 1 (2021), https://www.sciencedirect.com/science/article/pii/S2772656821000038.

[71] J. Zhang, Q. Zhang, X. Feng, Support and Interface Effects in Water-Splitting Electrocatalysts, Adv. Mater. 31 (2019) 1808167, https://onlinelibrary.wiley.com/doi/abs/10.1002/adma.201808167.

[72] N. Guillet, P. Millet, Alkaline Water Electrolysis, Hydrogen Production (2015) 117–166, https://onlinelibrary.wiley.com/doi/abs/10.1002/9783527676507.ch4.

[73] Y. Zheng, Y. Jiao, M. Jaroniec, S.Z. Qiao, Advancing the Electrochemistry of the Hydrogen-Evolution Reaction through Combining Experiment and Theory, Angew. Chem. Inter. Ed. 54 (2015) 52–65, https://onlinelibrary.wiley.com/doi/abs/10.1002/anie.201407031.

[74] D. Strmcnik, M. Uchimura, C. Wang, R. Subbaraman, N. Danilovic, D. van der Vliet, A.P. Paulikas, V.R. Stamenkovic, N.M. Markovic, Improving the hydrogen oxidation reaction rate by promotion of hydroxyl adsorption, Nat. Chem. 5 (2013) 300–306, https://doi.org/10.1038/nchem.1574.

[75] W. Sheng, Z. Zhuang, M. Gao, J. Zheng, J.G. Chen, Y. Yan, Correlating hydrogen oxidation and evolution activity on platinum at different pH with measured hydrogen binding energy, Nat. Commun. 6 (2015) 5848, https://doi.org/10.1038/ncomms6848.

[76] H. Sun, Z. Yan, F. Liu, W. Xu, F. Cheng, J. Chen, Self-Supported Transition-Metal-Based Electrocatalysts for Hydrogen and Oxygen Evolution, Adv. Mater. 32 (2020) 1806326, https://onlinelibrary.wiley.com/doi/abs/10.1002/adma.201806326.

[77] J.M. Gonçalves, T.A. Matias, K.C.F. Toledo, K. Araki, Electrocatalytic materials design for oxygen evolution reaction, in: R.v. Eldik, C. Hubbard (Eds.) Advances in Inorganic Chemistry, Elsevier, 2019, pp. 63.

[78] N.-T. Suen, S.-F. Hung, Q. Quan, N. Zhang, Y.-J. Xu, H.M. Chen, Electrocatalysis for the oxygen evolution reaction: recent development and future perspectives, Chem. Soc. Rev. 46 (2017) 337–365, https://doi.org/10.1039/C6CS00328A.

[79] Y. Wan, Z. Zhang, X. Xu, Z. Zhang, P. Li, X. Fang, K. Zhang, K. Yuan, K. Liu, G. Ran, Y. Li, Y. Ye, L. Dai, Engineering active edge sites of fractal-shaped single-layer $MoS_2$ catalysts for high-efficiency hydrogen evolution, Nano Energy 51 (2018) 786–792, https://www.sciencedirect.com/science/article/pii/S2211285518300958.

[80] L. Sun, Y. Zhang, Y. Zhang, H. Si, W. Qin, Y. Zhang, Reduced graphene oxide nanosheet modified NiMn-LDH nanoflake arrays for high-performance supercapacitors, Chem. Commun. 54 (2018) 10172–10175, https://doi.org/10.1039/C8CC05745A.

[81] A.-L. Yan, X.-C. Wang, J.-P. Cheng, Research Progress of NiMn Layered Double Hydroxides for Supercapacitors: A Review, Nanomater. 8 (2018).

[82] D.P. Dubal, P. Gomez-Romero, B.R. Sankapal, R. Holze, Nickel cobaltite as an emerging material for supercapacitors: An overview, Nano Energy 11 (2015) 377–399, https://www.sciencedirect.com/science/article/pii/S2211285514203077.

[83] A. Mohammadi Zardkhoshoui, B. Ameri, S. Saeed Hosseiny Davarani, α-$MnS@Co_3S_4$ hollow nanospheres assembled from nanosheets for hybrid supercapacitors, Chem. Eng. J. 422 (2021), https://www.sciencedirect.com/science/article/pii/S1385894721015370.

[84] Y. Wu, M. Yan, L. Sun, W. Shi, Flexible yolk-shelled $NiCo_2S_4$ hollow spheres/RGO film electrodes for efficient supercapacitive energy storage, New J. Chem. 42 (2018) 16174–16182, https://doi.org/10.1039/C8NJ03049A.

[85] R. Barik, P.P. Ingole, Challenges and prospects of metal sulfide materials for supercapacitors, Curr. Opin. Electrochem. 21 (2020) 327–334, https://www.sciencedirect.com/science/article/pii/S245191032030079X.

[86] J.M. Gonçalves, M.I. da Silva, M. Hasheminejad, H.E. Toma, K. Araki, P.R. Martins, L. Angnes, Recent Progress in Core@Shell Sulfide Electrode Materials for Advanced Supercapacitor Devices, Batteries & Supercaps 4 (2021) 1397, https://doi.org/10.1002/batt.202100017.

[87] J.M. Gonçalves, M.I. da Silva, H.E. Toma, L. Angnes, P.R. Martins, K. Araki, Trimetallic oxides/hydroxides as hybrid supercapacitor electrode materials: a review, J. Mater. Chem. A 8 (2020) 10534–10570, https://doi.org/10.1039/D0TA02939D.

[88] V. Quispe-Garrido, G.A. Cerron-Calle, A. Bazan-Aguilar, J.G. Ruiz-Montoya, E. O. López, A.M. Baena-Moncada, Advances in the design and application of transition metal oxide-based supercapacitors, Open Chem. 19 (2021) 709–725, https://doi.org/10.1515/chem-2021-0059.

[89] S. Ding, J. An, D. Ding, Y. Zou, L. Zhao, Micron-sized NiMn-glycerate solid spheres as cathode materials for all-solid-state asymmetric supercapacitor with superior energy density and cycling life, Chem. Eng. J. 431 (2022), https://www.sciencedirect.com/science/article/pii/S1385894721056746.

[90] F.-X. Ma, H. Hu, H.B. Wu, C.-Y. Xu, Z. Xu, L. Zhen, X.W. Lou, Formation of Uniform Fe3O4 Hollow Spheres Organized by Ultrathin Nanosheets and Their Excellent Lithium Storage Properties, Adv. Mater. 27 (2015) 4097–4101, https://doi.org/10.1002/adma.201501130.

[91] J. Wang, B. Wang, X. Liu, G. Wang, H. Wang, J. Bai, Construction of carbon-coated nickel phosphide nanoparticle assembled submicrospheres with enhanced electrochemical properties for lithium/sodium-ion batteries, J Colloid Interf Sci, 538 (2019) 187-198. https://www.sciencedirect.com/science/article/pii/S0021979718314152.

[92] Y. Wang, L. Yu, X.W. Lou, Synthesis of Highly Uniform Molybdenum-Glycerate Spheres and Their Conversion into Hierarchical $MoS_2$ Hollow Nanospheres for

Lithium-Ion Batteries, Angew. Chem. Int. Ed. 55 (2016) 7423–7426, https://doi.org/10.1002/anie.201601673.
[93] Y. Wang, L. Yu, X.W. Lou, Formation of Triple-Shelled Molybdenum-Polydopamine Hollow Spheres and Their Conversion into $MoO_2$/Carbon Composite Hollow Spheres for Lithium-Ion Batteries, Angew. Chem. Int. Ed. 55 (2016) 14668–14672, https://doi.org/10.1002/anie.201608410.
[94] Z. Wang, D.K. Denis, Z. Zhao, X. Sun, J. Zhang, L. Hou, C. Yuan, Unusual formation of hollow $NiCoO_2$ sub-microspheres by oxygen functional group dominated thermally induced mass relocation towards efficient lithium storage, J. Mater. Chem. A 7 (2019) 18109–18117, https://doi.org/10.1039/C9TA06432J.
[95] L. Zhu, H. Lu, F. Xiao, T. Yao, T. Liu, F. Li, J. Wang, X. Han, Y. Cheng, H. Wang, Flower-like Mn/Co Glycerolate-Derived α-MnS/$Co_9S_8$/Carbon Heterostructures for High-Performance Lithium-Ion Batteries, ACS Appl. Energy Mater. 3 (2020) 10215–10223, https://doi.org/10.1021/acsaem.0c02014.
[96] A. Amiri, R. Shahbazian-Yassar, Recent progress of high-entropy materials for energy storage and conversion, J. Mater. Chem. A 9 (2021) 782–823, https://doi.org/10.1039/D0TA09578H.
[97] J. Lin, L. Zhu, S. Chen, Q. Li, Z. He, Z. Cai, L. Cao, Z. Yuan, J. Liu, Self-Templated Formation of Hollow Yolk-Like Spheres Iron Fluoride as Cathode Material for High-Performance Li-Ion Batteries, J Electrochem Soc, 166 (2019) A2074-A2082. http://dx.doi.org/10.1149/2.0991910jes.
[98] S. Li, C. Li, W.K. Pang, Z. Zhao, J. Zhang, Z. Liu, D. Li, Engineering Unique Ball-In-Ball Structured $(Ni_{0.33}Co_{0.67})_9S_8$@C Nanospheres for Advanced Sodium Storage, Acs Appl Mater Inter 11 (2019) 27805–27812, https://doi.org/10.1021/acsami.9b07214.
[99] X. Zhang, Y. Zhou, B. Luo, H. Zhu, W. Chu, K. Huang, Microwave-Assisted Synthesis of $NiCo_2O_4$ Double-Shelled Hollow Spheres for High-Performance Sodium Ion Batteries, Nano-Micro Lett 10 (2017) 13, https://doi.org/10.1007/s40820-017-0164-2.
[100] R. Wang, Z. Li, G. Xu, X. Liu, Y. Huang, X. Wei, L. Yang, Yolk-shell spheres constructed of ultrathin $MoSe_2$ nanosheets as a high-performance anode for sodium dual ion batteries, Solid State Ion. 353 (2020), https://www.sciencedirect.com/science/article/pii/S0167273819312202.
[101] L. Shen, Y. Wang, F. Wu, I. Moudrakovski, P.A. van Aken, J. Maier, Y. Yu, Hierarchical Metal Sulfide/Carbon Spheres: A Generalized Synthesis and High Sodium-Storage Performance, Angew. Chem. Int. Ed. 58 (2019) 7238–7243, https://doi.org/10.1002/anie.201901840.
[102] J. Wang, L. Zhu, F. Li, T. Yao, T. Liu, Y. Cheng, Z. Yin, H. Wang, Synergizing Phase and Cavity in $CoMoO_xS_y$ Yolk-Shell Anodes to Co-Enhance Capacity and Rate Capability in Sodium Storage, Small 16 (2020) 2002487, https://doi.org/10.1002/smll.202002487.
[103] S.H. Choi, Y.C. Kang, Synergetic Effect of Yolk-Shell Structure and Uniform Mixing of SnS–$MoS_2$ Nanocrystals for Improved Na-Ion Storage Capabilities, Acs Appl Mater Inter 7 (2015) 24694–24702, https://doi.org/10.1021/acsami.5b07093.
[104] Y. Guo, T. Park, J.W. Yi, J. Henzie, J. Kim, Z. Wang, B. Jiang, Y. Bando, Y. Sugahara, J. Tang, Y. Yamauchi, Nanoarchitectonics for Transition-Metal-Sulfide-Based Electrocatalysts for Water Splitting, Adv. Mater. 31 (2019) 1807134, https://doi.org/10.1002/adma.201807134.
[105] C.G. Morales-Guio, L.-A. Stern, X. Hu, Nanostructured hydrotreating catalysts for electrochemical hydrogen evolution, Chem. Soc. Rev. 43 (2014) 6555–6569, https://doi.org/10.1039/C3CS60468C.
[106] J. Zhu, L. Hu, P. Zhao, L.Y.S. Lee, K.-Y. Wong, Recent Advances in Electrocatalytic Hydrogen Evolution Using Nanoparticles, Chem. Rev. 120 (2020) 851–918, https://doi.org/10.1021/acs.chemrev.9b00248.
[107] X. Zou, Y. Zhang, Noble metal-free hydrogen evolution catalysts for water splitting, Chem. Soc. Rev. 44 (2015) 5148–5180, https://doi.org/10.1039/C4CS00448E.
[108] S.V. Mohite, R. Xing, B. Li, S.S. Latthe, Y. Zhao, X. Li, L. Mao, S. Liu, Spatial Compartmentalization of Cobalt Phosphide in P-Doped Dual Carbon Shells for Efficient Alkaline Overall Water Splitting, Inorg. Chem. 59 (2020) 1996–2004, https://doi.org/10.1021/acs.inorgchem.9b03363.
[109] X. Guo, J. Liang, L. Wang, Z. Feng, T. Yu, Z. Zhang, Y. Shao, C. Hao, G. Li, Synthesis of Cobalt-Glycerate hierarchical structure and their conversion into hierarchical CoP nanospheres for the hydrogen evolution reaction, Int J Hydrogen Energ 43 (2018) 2034–2042, https://www.sciencedirect.com/science/article/pii/S0360319917346918.
[110] X. Liu, S. Deng, D. Xiao, M. Gong, J. Liang, T. Zhao, T. Shen, D. Wang, Hierarchical Bimetallic Ni–Co–P Microflowers with Ultrathin Nanosheet Arrays for Efficient Hydrogen Evolution Reaction over All pH Values, Acs Appl Mater Inter 11 (2019) 42233–42242, https://doi.org/10.1021/acsami.9b15194.
[111] X. Liu, S. Deng, P. Liu, J. Liang, M. Gong, C. Lai, Y. Lu, T. Zhao, D. Wang, Facile self-template fabrication of hierarchical nickel-cobalt phosphide hollow nanoflowers with enhanced hydrogen generation performance, Sci. Bull. 64 (2019) 1675–1684, https://www.sciencedirect.com/science/article/pii/S2095927319305559.
[112] Z. Zhou, Z. Pei, L. Wei, S. Zhao, X. Jian, Y. Chen, Electrocatalytic hydrogen evolution under neutral pH conditions: current understandings, recent advances, and future prospects, Energ, Environ. Sci. 13 (2020) 3185–3206, https://doi.org/10.1039/D0EE01856B.
[113] J.M. Gonçalves, M. Ireno da Silva, L. Angnes, K. Araki, Vanadium-containing electro and photocatalysts for the oxygen evolution reaction: a review, J. Mater. Chem. A 8 (2020) 2171–2206, https://doi.org/10.1039/C9TA10857B.
[114] S.N.F. Moridon, K. Arifin, R.M. Yunus, L.J. Minggu, M.B. Kassim, Photocatalytic water splitting performance of $TiO_2$ sensitized by metal chalcogenides: A review, Ceram. Int. 48 (2022) 5892–5907, https://www.sciencedirect.com/science/article/pii/S0272884221036233.
[115] J. Huang, X. Ma, Y. Sun, L. Wang, H. She, J. Li, Q. Wang, Preparation of $Zn_{0.5}Cd_{0.5}S$@Ni-Glycerate composite for photocatalytic water reduction, Mat Sci Semicon Proc 105 (2020) 104703. https://www.sciencedirect.com/science/article/pii/S1369800119314283.
[116] M.R. Gholipour, C.C. Nguyen, F. Béland, T.-O. Do, Hollow microspheres consisting of uniform $Zn_xCd_{1-x}S$ nanoparticles with noble-metal-free co-catalysts for hydrogen evolution with high quantum efficiency under visible light, J. Photochem. Photobiol. A Chem. 358 (2018) 1–9, https://www.sciencedirect.com/science/article/pii/S1010603017317938.
[117] Y.V. Kaneti, Y. Guo, N.L.W. Septiani, M. Iqbal, X. Jiang, T. Takei, B. Yuliarto, Z.A. Alothman, D. Golberg, Y. Yamauchi, Self-templated fabrication of hierarchical hollow manganese-cobalt phosphide yolk-shell spheres for enhanced oxygen evolution reaction, Chem. Eng. J. 405 (2021), https://www.sciencedirect.com/science/article/pii/S138589472032708X.
[118] N.-H. Ting, T.X. Nguyen, C.-H. Lee, Y.-C. Chen, C.-H. Yeh, H.-Y.-T. Chen, J.-M. Ting, Composition-controlled high entropy metal glycerate as high-performance electrocatalyst for oxygen evolution reaction, Appl. Mater. Today 27 (2022), https://www.sciencedirect.com/science/article/pii/S2352940722000373.
[119] W. Song, X. Teng, Y. Niu, S. Gong, X. He, Z. Chen, Self-templating construction of hollow Fe-CoxP nanospheres for oxygen evolution reaction, Chem. Eng. J. 409 (2021), https://www.sciencedirect.com/science/article/pii/S1385894720343436.
[120] H. Wang, E.-M. Feng, Y.-M. Liu, C.-Y. Zhang, High-performance hierarchical ultrathin sheet-based CoOOH hollow nanospheres with rich oxygen vacancies for the oxygen evolution reaction, J. Mater. Chem. A 7 (2019) 7777–7783, https://doi.org/10.1039/C9TA00878K.
[121] N.L.W. Septiani, Y.V. Kaneti, K.B. Fathoni, Y. Guo, Y. Ide, B. Yuliarto, X. Jiang, H. K. Nugraha, D. Dipojono, Y.Y. Golberg, Tailorable nanoarchitecturing of bimetallic nickel–cobalt hydrogen phosphate via the self-weaving of nanotubes for efficient oxygen evolution, J. Mater. Chem. A 8 (2020) 3035–3047, https://doi.org/10.1039/C9TA13442E.
[122] T.X. Nguyen, Y.-H. Su, C.-C. Lin, J. Ruan, J.-M. Ting, A New High Entropy Glycerate for High Performance Oxygen Evolution Reaction, Adv. Sci. 8 (2021) 2002446, https://doi.org/10.1002/advs.202002446.
[123] N.L.W. Septiani, Y.V. Kaneti, K.B. Fathoni, K. Kani, A.E. Allah, B. Yuliarto, H.K. Nugraha, Z.A. Dipojono, D. Alothman, Y.Y. Golberg, Self-Assembly of Two-Dimensional Bimetallic Nickel-Cobalt Phosphate Nanoplates into One-Dimensional Porous Chainlike Architecture for Efficient Oxygen Evolution Reaction, Chem. Mater. 32 (2020) 7005–7018, https://doi.org/10.1021/acs.chemmater.0c02385.
[124] N.L.W. Septiani, Y.V. Kaneti, Y. Guo, B. Yuliarto, X. Jiang, Y. Ide, N. Nugraha, H. K. Dipojono, A. Yu, Y. Sugahara, D. Golberg, Y. Yamauchi, Holey Assembly of Two-Dimensional Iron-Doped Nickel-Cobalt Layered Double Hydroxide Nanosheets for Energy Conversion Application, ChemSusChem n/a (2019), https://doi.org/10.1002/cssc.201901364.
[125] Z. Dong, W. Zhang, Y. Xiao, Y. Wang, C. Luan, C. Qin, Y. Dong, M. Li, X. Dai, X. Zhang, One-Pot-Synthesized CoFe-Glycerate Hollow Spheres with Rich Oxyhydroxides for Efficient Oxygen Evolution Reaction, ACS Sustain. Chem. Eng. 8 (2020) 5464–5477, https://doi.org/10.1021/acssuschemeng.9b06579.
[126] N. Han, P. Liu, J. Jiang, L. Ai, Z. Shao, S. Liu, Recent advances in nanostructured metal nitrides for water splitting, J. Mater. Chem. A 6 (2018) 19912–19933, https://doi.org/10.1039/C8TA06529B.
[127] A. Dutta, N. Pradhan, Developments of Metal Phosphides as Efficient OER Precatalysts, J. Phys. Chem. Lett. 8 (2017) 144–152, https://doi.org/10.1021/acs.jpclett.6b02249.
[128] W.T. Hong, M. Risch, K.A. Stoerzinger, A. Grimaud, J. Suntivich, Y. Shao-Horn, Toward the rational design of non-precious transition metal oxides for oxygen electrocatalysis, Energ, Environ. Sci. 8 (2015) 1404–1427, https://doi.org/10.1039/C4EE03869J.
[129] F. Song, L. Bai, A. Moysiadou, S. Lee, C. Hu, L. Liardet, X. Hu, Transition Metal Oxides as Electrocatalysts for the Oxygen Evolution Reaction in Alkaline Solutions: An Application-Inspired Renaissance, J. Am. Chem. Soc. 140 (2018) 7748–7759, https://doi.org/10.1021/jacs.8b04546.
[130] J.M. Gonçalves, P.R. Martins, L. Angnes, K. Araki, Recent advances in ternary layered double hydroxide electrocatalysts for the oxygen evolution reaction, New J. Chem. 44 (2020) 9981–9997, https://doi.org/10.1039/D0NJ00021C.
[131] Z. Cai, X. Bu, P. Wang, J.C. Ho, J. Yang, X. Wang, Recent advances in layered double hydroxide electrocatalysts for the oxygen evolution reaction, J. Mater. Chem. A 7 (2019) 5069–5089, https://doi.org/10.1039/C8TA11273H.
[132] Q. Hu, G. Li, Z. Han, Z. Wang, X. Huang, H. Yang, Q. Zhang, J. Liu, C. He, Recent progress on the hybrids of transition metals/carbon for electrochemical water splitting, J. Mater. Chem. A (2019), https://doi.org/10.1039/C9TA04163J.
[133] J.M. Gonçalves, T.A. Matias, L.P.H. Saravia, M. Nakamura, J.S. Bernardes, M. Bertotti, K. Araki, Synergic effects enhance the catalytic properties of alpha-Ni$(OH)_2$-FeOCPc@rGO composite for oxygen evolution reaction, Electrochim Acta, 267 (2018) 161-169. http://www.sciencedirect.com/science/article/pii/S0013468618303712.
[134] X. Li, A.M. Elshahawy, C. Guan, J. Wang, Metal Phosphides and Phosphates-based Electrodes for Electrochemical Supercapacitors, Small 13 (2017) 1701530, https://doi.org/10.1002/smll.201701530.

[135] J. Huang, J. Chen, T. Yao, J. He, S. Jiang, Z. Sun, Q. Liu, W. Cheng, F. Hu, Y. Jiang, Z. Pan, S. Wei, CoOOH Nanosheets with High Mass Activity for Water Oxidation, Angew. Chem. Int. Ed. 54 (2015) 8722–8727, https://doi.org/10.1002/anie.201502836.
[136] J.M. Gonçalves, I.S. Lima, N.F.B. Azeredo, D.P. Rocha, A. de Siervo, L. Angnes, NiVCe-Layered Double Hydroxide as Multifunctional Nanomaterials for Energy and Sensor Applications, Front. Mater., 8 (2021). https://www.frontiersin.org/article/10.3389/fmats.2021.781900.
[137] A. Karmakar, K. Karthick, S.S. Sankar, S. Kumaravel, R. Madhu, S. Kundu, A vast exploration of improvising synthetic strategies for enhancing the OER kinetics of LDH structures: a review, J. Mater. Chem. A 9 (2021) 1314–1352, https://doi.org/10.1039/D0TA09788H.
[138] L. Mohapatra, K. Parida, A review on the recent progress, challenges and perspective of layered double hydroxides as promising photocatalysts, J. Mater. Chem. A 4 (2016) 10744–10766, https://doi.org/10.1039/C6TA01668E.
[139] P.d.O. Rossini, A. Laza, N.F.B. Azeredo, J.M. Gonçalves, F.S. Felix, K. Araki, L. Angnes, Ni-based double hydroxides as electrocatalysts in chemical sensors: A review, Trends Analyt Chem, 126 (2020) 115859. http://www.sciencedirect.com/science/article/pii/S0165993620300881.
[140] Y. Wang, Y. Zhang, Z. Liu, C. Xie, S. Feng, D. Liu, M. Shao, S. Wang, Layered Double Hydroxide Nanosheets with Multiple Vacancies Obtained by Dry Exfoliation as Highly Efficient Oxygen Evolution Electrocatalysts, Angew. Chem. Int. Ed. 56 (2017) 5867–5871, https://doi.org/10.1002/anie.201701477.
[141] M.S. Burke, L.J. Enman, A.S. Batchellor, S. Zou, S.W. Boettcher, Oxygen Evolution Reaction Electrocatalysis on Transition Metal Oxides and (Oxy) hydroxides: Activity Trends and Design Principles, Chem. Mater. 27 (2015) 7549–7558, https://doi.org/10.1021/acs.chemmater.5b03148.
[142] S. Klaus, Y. Cai, M.W. Louie, L. Trotochaud, A.T. Bell, Effects of Fe Electrolyte Impurities on $Ni(OH)_2$/NiOOH Structure and Oxygen Evolution Activity, J. Phys. Chem. C 119 (2015) 7243–7254, https://doi.org/10.1021/acs.jpcc.5b00105.
[143] D. Friebel, M.W. Louie, M. Bajdich, K.E. Sanwald, Y. Cai, A.M. Wise, M.-J. Cheng, D. Sokaras, T.-C. Weng, R. Alonso-Mori, R.C. Davis, J.R. Bargar, J.K. Nørskov, A. Nilsson, A.T. Bell, Identification of Highly Active Fe Sites in (Ni, Fe) OOH for Electrocatalytic Water Splitting, J. Am. Chem. Soc. 137 (2015) 1305–1313, https://doi.org/10.1021/ja511559d.
[144] T.G. Ritter, A.H. Phakatkar, M.G. Rasul, M.T. Saray, L.V. Sorokina, T. Shokuhfar, J.M. Gonçalves, R. Shahbazian-Yassar, Electrochemical synthesis of high entropy hydroxides and oxides boosted by hydrogen evolution reaction, Cell Rep. Phys. Sci., 3 (2022) 100847. https://www.sciencedirect.com/science/article/pii/S2666386422001217.
[145] H. Han, H. Choi, S. Mhin, Y.-R. Hong, K.M. Kim, J. Kwon, G. Ali, K.Y. Chung, M. Je, H.N. Umh, D.-H. Lim, K. Davey, S.-Z. Qiao, U. Paik, T. Song, Advantageous crystalline–amorphous phase boundary for enhanced electrochemical water oxidation, Energ, Environ. Sci. 12 (2019) 2443–2454, https://doi.org/10.1039/C9EE00950G.
[146] Y. Dahiya, M. Hariram, M. Kumar, A. Jain, D. Sarkar, Modified transition metal chalcogenides for high performance supercapacitors: Current trends and emerging opportunities, Coord. Chem. Rev., 451 (2022) 214265. https://www.sciencedirect.com/science/article/pii/S0010854521005397.
[147] P. García Lebière, A. Pérez del Pino, C. Logofatu, E. György, Laser synthesis of NixZnyO/reduced graphene oxide/carbon nanotube electrodes for energy storage applications, Appl Surf Sci, 563 (2021) 150234. https://www.sciencedirect.com/science/article/pii/S0169433221013106.
[148] D.P. Rocha, V.N. Ataide, A. de Siervo, J.M. Gonçalves, R.A.A. Muñoz, T.R.L.C. Paixão, L. Angnes, Reagentless and sub-minute laser-scribing treatment to produce enhanced disposable electrochemical sensors via additive manufacture, Chem. Eng. J, 425 (2021) 130594. https://www.sciencedirect.com/science/article/pii/S138589472102180X.